DEPARTMENT OF PHYSICS
UNIVERSITY OF JYVÄSKYLÄ
RESEARCH REPORT No. 8/2009

THERMAL PROPERTIES IN LOW DIMENSIONAL STRUCTURES BELOW 1 K

BY
JENNI KARVONEN

Academic Dissertation
for the Degree of
Doctor of Philosophy

To be presented, by permission of the
Faculty of Mathematics and Science
of the University of Jyväskylä,
for public examination in Auditorium FYS-1 of the
University of Jyväskylä on September 4, 2009
at 12 o'clock noon

Jyväskylä, Finland
September, 2009

Preface

The work reviewed in this thesis has been carried out during the years 2004-2009 at the Department of Physics and Nanoscience Center in the University of Jyväskylä.

First of all, I would like to thank my supervisor Professor Ilari Maasilta for guidance and support during all these years starting from summer 2001, when I came to his door as a summer student. I believe that without our fruitful co-operation, I would not have had enough faith and courage even to aim toward this goal. I also want to thank all former and present members of our group, Physics Department's and Nanoscience center's staff . Especially I want to thank Dr. Panu Koppinen, Ms. Minna Nevala, Mr. Tero Isotalo, Mr. Kimmo Kinnunen, Dr. Thomas Kühn, Ms. Terhi Hongisto, Dr. Lasse Taskinen, Dr. Jani Kivioja, Mr. Harri Niiranen, Mr. Jaakko Halkosaari and our Laboratory engineers Mr. Antti Nuottajärvi and Mr. Tarmo Suppula.

Financial support from Vilho, Yrjö and Kalle Väisälä Foundation, Magnus Ehnrooth foundation and Ellen and Artturi Nyyssönen foundation are gratefully acknowledged.

I wish to thank my parents, Tapani and Riitta, siblings, Henna and Teemu, other relatives and friends for their support. Warm thanks also go to Leo-ukki and Irja-mummo. Finally, I thank Matti for his love and support as well as discussions about physics and his patience to explain for me the wonders of physics from a theoretician point of view.

Jyväskylä, September 2009

Jenni Karvonen

Abstract

Karvonen, Jenni
Thermal properties in low dimensional structures
Jyväskylä: University of Jyväskylä, 2009, 114 p.
(Research report/Department of Physics, University of Jyväskylä,
ISSN 0075-465X; 8/2009)
ISBN 978-951-39-3583-2
diss.

In this thesis thermal properties of low dimensional structures were experimentally studied at low temperatures with the help of tunnel junction thermometry and the Joule heating technique. The main objects of study were electron-phonon coupling in disordered thin metal films and phonon transport in suspended silicon nitride membranes. Our aim has been to clarify the effect of the phonon dimensionality, *i.e.* the effect of boundaries to the phonon modes and the transition from 3D to 2D phonons. The dimensionality cross over had not been observed before this work even though it is fabricationally a standard procedure to create the low dimensional environments for nanoscale applications and devices. The main conclusion here is that the nature of thermal phenomena can differ drastically in lower dimensional structures compared to bulk behaviour, and sometimes surprisingly advantageous ways.

Keywords Thermal relaxation, electron-phonon coupling, phonon transport, low dimensional structures, SINIS thermometry

Author's address	Jenni Karvonen Nanoscience Center Department of Physics University of Jyväskylä Finland
Supervisor	Professor Ilari Maasilta Nanoscience Center Department of Physics University of Jyväskylä Finland
Reviewers	Professor Kurt Gloos Wihuri Physical Laboratory Department of Physics University of Turku Finland
Reviewers	Dr. Matthias Meschke Low Temperature Laboratory Helsinki University of Technology Finland
Opponent	Professor Christian Enss Kirchhoff-Institute for Physics University of Heidelberg Germany

List of Publications

The main results of this thesis have been reported in the following articles:

A.I. J.T. Karvonen, L.J. Taskinen and I.J. Maasilta, *Observation of disorder-indused weakening of electron-phonon interaction in thin nobel metal films*. Phys. Rev. B **72** (2005) 012302.

A.II. J.T. Karvonen, L.J. Taskinen and I.J. Maasilta, *Influence of temperature gradients on tunnel junction thermometry below 1 K*. J. Low Temp. Phys. **149** (2007) 121.

A.III. J.T. Karvonen and I.J. Maasilta, *Influence of phonon dimensionality on electron energy relaxation*. Phys. Rev. Lett. **99** (2007) 145503.

A.IV. J.T. Karvonen and I.J. Maasilta, *Observation of phonon dimensionality effects on electron energy relaxation*. J. Phys.: Conf. Series **92** (2007) 012043.

A.V. J.T. Karvonen, T. Kühn and I.J. Maasilta, *Phonon transport in suspended silicon nitride membranes at low temperatures*. J. Phys.: Conf. Series **150** (2009) 012019.

Author's contribution

The applicant has carried out the sample fabrication, performed the measurements and the data analysis in all the papers except in paper A.II., where the numerical simulations and AlMn measurements were performed by others. She made a major contribution in the writing process of all the papers, which was done together with Prof. I. Maasilta.

Other publications to which the author has contributed

B.I. J.M. Kivioja, I.J. Maasilta, J.P. Pekola and J.T. Karvonen, *Response time of a thermometer based on normal metal-insulator-superconductor (NIS) tunnel junctions*. Physica E **18** (2003) 21–22.

B.II. L.J. Taskinen, J.T. Karvonen, J.M. Kivioja and I.J. Maasilta, *Measuring the electron-phonon interaction with NIS junction: direct measurement of the scattering rate*. Phys. Stat. Sol. (c) **1** (2004) 2856–2859.

B.III. J.T. Karvonen, L.J. Taskinen and I.J. Maasilta, *Electron-phonon interaction in thin copper and gold films*. Phys. Stat. Sol. (c) **1** (2004) 2799–2802.

B.IV. L.J. Taskinen, J.T. Karvonen and I.J. Maasilta, *Electron-phonon interaction in a thin Al-Mn film*. Nucl. Instr. and Meth. **559** (2006) 706.

B.V. P.J. Koppinen, J.T. Karvonen, L.J. Taskinen and I.J. Maasilta, *Thermal conduction in nanostructures by virtual photons*. AIP Conf. Proc. **850** (2006) 1556.

Contents

Chapter 1

Introduction

Temperature is an important quantity both in everyday life and science. At the macroscopic level, the definition of temperature is based on a concept of thermal equilibrium and the zeroth law of thermodynamics [1]. According to the zeroth law, if the pairs of objects A and B and B and C are in thermal equilibrium, we can conclude that also the objects A and C are in an equilibrium state. Therefore, all systems A, B, and C can be described by the same value of a property, which we call temperature. On the other hand, temperature can be considered as the average kinetic energy per each degree of freedom at the microscopic level. For example in solids, due to the thermal energy atoms vibrate in the lattice around their equilibrium positions and the quantized vibration modes are called phonons [1].

In a nonequilibrium state, systems have a tendency to equalize their temperatures, which is observed as a flow of energy. From this imbalance rise several crucial phenomena, such as thermal relaxation and thermal conductivity, which describe many thermal properties of a system or a material. When nano- or mesoscopic solid state devices such as coolers [2], bolometric radiation detectors [3,4] or quantum bits are studied at low temperatures and in different kind of surroundings, the thermal properties can be in a limiting role for their operations, even though detailed understanding of these properties is lacking in many case. This is in contrast to the optical and electrical properties of nanoscale devices, which have gain plenty of scientific attention during the last decades. The main reason for this trend is that temperature, which is the key quantity for defining any thermal properties, is challenging to measure reliably. The task is even harder in nanoscale structures at low temperatures, when a very weak thermal coupling enables the conduction electrons and the lattice to be at significantly different temperatures in a nonequilibrium state.

In this work, electron-phonon (e-p) coupling in metal wires and phonon transport in suspended silicon nitride membranes are experimentally studied at sub-Kelvin temperatures. The idea is to compare the behavior of these phenomena in a case of both three and two dimensional phonons, and to observe the effects of phonon dimensionality. The phenomena are studied by using the Joule heating technique and tunnel junction thermometry. The choice of thermometry is critical to achieve the goals of this work, and therefore sensitive *normal metal-insulator-superconductor* (NIS) tunnel junction thermometers are used to measure temperature below 1 K. A NIS tunnel junction measures directly the local electron temperature of a normal metal without dissipating a significant amount of extra heat. In addition, they are also easily integrated to nano- and mesoscopic structures, which makes them useful thermometers in nanoscale applications and devices.

This work is organized in a following way. In chapter 2 the sample fabrication methods and the measurement set-up are discussed in a general level. Next, tunnel junction thermometry is discussed in chapter 3. One of the main subjects of this thesis is the electron-phonon coupling and theoretical results of it are briefly introduced in chapter 4. In chapter 5, numerical and experimental results on thermal gradients in mesoscopic copper and aluminum manganese thin films on bulk substrate, below 1 Kelvin with a non-uniform Joule heating technique, are presented [I, II]. In chapter 6, the experimental results of the electron-phonon coupling measurements in the case of both 3D and 2D phonons are discussed [III, IV]. We show that the temperature dependence and the strength of the electron-phonon coupling indeed changes as the phonon dimensionality is decreased. Also, the effect of increasing disorder, *i.e.* decreasing electron mean free path, on the e-p coupling in Cu thin films on bulk and membrane substrates was measured, and the results are presented in chapter 6. The second main topic of this thesis is phonon transport in suspended silicon nitride membranes, which is discussed in chapter 7 [V]. We have studied heat transport in SiN_x membranes with different thicknesses ranging from 40 to 750 nm, by using a radially symmetric thin film heater, and measuring the local phonon temperature with a SINIS thermometer at various distances from the heater. Finally, the results are summarized in chapter 8.

Chapter 2

Sample fabrication and measurement setup

In this chapter, the essential fabrication methods and the measurement set-up used in this thesis are presented. All metallic structures studied in this work have been fabricated by using conventional electron beam lithography and a multi-angle evaporation technique, which are discussed first in section 2.1. The suspended silicon nitride membranes, on the other hand, are fabricated by using optical lithography and wet etching, as discussed in section 2.2. In the measurements presented in this work, a He^3-He^4 dilution refrigerator was used to achieve the cryogenic temperatures. The measurement setup including electronics, is discussed in section 2.3 in a general level.

2.1 Electron beam lithography and multi-angle evaporation techniques

All metallic structures of the samples studied in this work have been fabricated by using conventional electron beam lithography and evaporation techniques [5,6]. In electron beam lithography, the double layer resist method is used to achieve a large enough undercut profile, which is essential for the lift-off processes and in the fabrication of tunnel junctions.

A commonly used bulk substrate in micro- and nanofabrication is silicon (Si), which is usually coated by insulating layer such as silicon oxide (SiO_2) or nitride (Si_3N_4). Before processing steps, the substrate needs to be cleaned carefully. A chip, cut from a wafer, is set in hot acetone and scrubbed with a cotton stick to remove large particles. Next, cleaning is continued in ultrasonic bath, which effectively removes smaller particles. Finally, the chip is rinsed with isopropanol and dried with

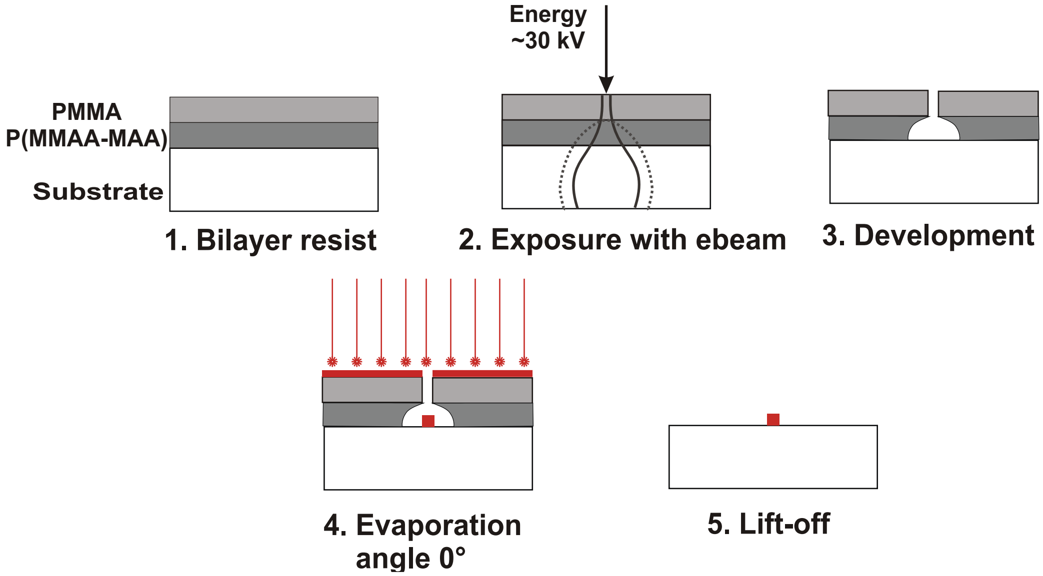

Figure 2.1 Fabrication of metallic structures by using positive electron beam lithography and evaporation techniques. Bilayer resist is used to achieve the undercut structure shown in step 3.

nitrogen gas.

Electron beam resists used in this work are polymethyl methacrylate (PMMA 950 MW) in chlorobenzene or anisole and a mixture of PMMA and 8.5 % methacrylic acid (P(MMA-MAA)) in acetic acid or ethyle lactate. Resists are spun for $\sim$ 1 min with a speed of 2000-6000 rpm depending on the desired resist thickness. After each spinning, the resist is baked on a hot plate at $\sim$ 170 °C from 1 to 30 min depending on the type of resist (Fig. 2.1 step 1.). Patterning is done by using scanning electron microscope (LEO 1430), which has a lanthanum hexaboride (LaB_6) electron source, a beam blanker and computer software to control the motorized stage and the blanker. The acceleration voltage used is $\sim$ 30 kV, which produces the electron scattering profile presented schematically in figure 2.1 in step 2. The inner profile, marked by the solid line, is due to primary electrons and the outer profile, marked by the dotted line, is due to secondary electrons. Because the secondary electrons don't reach the top resist, *i. e.* PMMA, narrow linewidth and a large enough undercut enables the fabrication of a suspended bridge structure, which is essential for multi-angle evaporation.

After exposure, reacted parts of the resist are removed by developers, which dissolve the resist. First, the chip is set into a mixture of methylisobutylketon (MIBK) and isopropanol (1:2) for $\sim$ 45 s, and second, into a solution of methyl glycol and methanol (1:2) for $\sim$ 10 s. The developers are flushed away with isopropanol and the

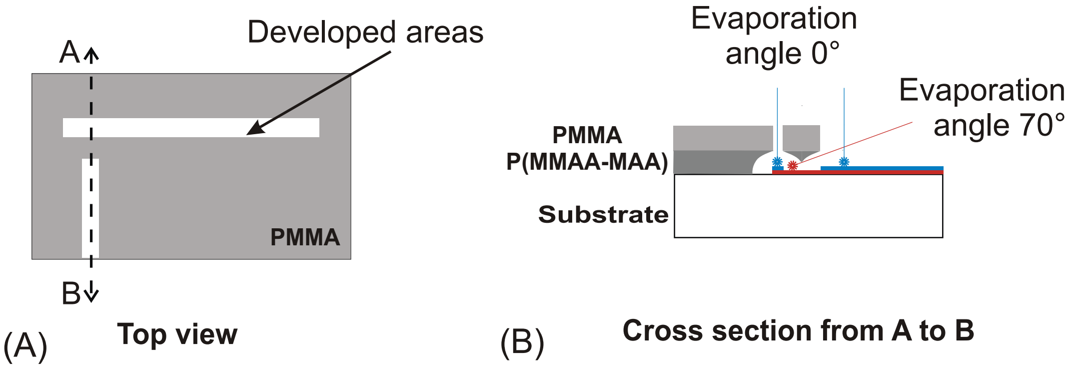

Figure 2.2 Schematic picture of the multiangle evaporation technique with help of an undercut structure.

chip is dried with nitrogen gas after each development. The first developer removes exposed parts of the resists in the both layers, but the second developer dissolves only P(MMA-MAA) also from the unexposed areas, resulting in the undercut profile shown in Fig. 2.1 step 3.

Before metal deposition (Fig. 2.1 step 4.), the surface of the chip from developed areas is cleaned of organic residues with oxygen plasma in a reactive ion etcher (RIE) (Plasmalab 80Plus, Oxfrod Instruments) for 30 s at 40 mTorr with 50 sccm flow of oxygen and 30 W RF-power. Immediately after the oxygen plasma cleaning, the chip is moved to the loading chamber of an evaporator and pumped to vacuum. The evaporator chamber is pumped with a cryopump (Cryo-Torr High Vacuum pump, CTI-Cryogenics) and its base pressure is $\sim 10^{-9}$ mbar. Evaporation angles can be changed by rotating and tilting the sample stage in vacuum, and oxidations can be done *in situ* in the loading chamber. The evaporation rate depends on evaporated metal. For example for Al and Cu the rate is 0.1-0.2 nm/s, but for Nb 0.3-0.5 nm/s due to the better film quality. In figure 2.2 an example of multiangle evaporation process is shown, in which the stage is tilted at a large angle (red metal) during the first evaporation and the second evaporation is done at zero angle (blue metal).

After deposition, the extra resist with the metal on top is dissolved in a *lift-off* process, in which the chip is immersed in a warm acetone. Finally, the chip is rinsed with isopropanol and dried with nitrogen gas. The result after lift-off is shown in the figure 2.1 in step 5.

2.2 Fabrication of suspended silicon nitride membranes

The silicon nitride membranes used in this work are fabricated by using positive photolithography and anisotropic wet etching of (100) oriented silicon wafers (thickness 300-500 μm) with aqueous KOH solution. In Fig. 2.3, the main steps of the fabrication process are shown. On both sides of the wafer, low-stress silicon nitride (SiN_x thickness 30, 200, 750 nm) was grown by Low Pressure Chemical Vapor Deposition (LPCVD) at the UC Berkeley Microfabrication Laboratory. Before spinning the resist, the chips are cleaned in a similar way to the case of electron beam lithography explained in Section 2.1. The photoresist used is AZ1514H and it was usually spun at a speed of $\sim$ 2000 rpm and baked at 100 °C for 1 minute.

Figure 2.3 Fabrication of silicon nitride membranes by positive photolithography and wet etching of (100) silicon. (a) The chip after developing the photoresist (red) from exposed areas. (b) Silicon nitride (green) is removed with a reactive ion etcher. (c) Crystalline silicon is anisotropically wet etched in aqueous KOH. The etch rate is orders of magnitude slower in the direction of <111> [6], resulting in the profile shown.

Exposure is done by using a mask aligner (Karl Suss KG, SUSS MA 45) with a mercury lamp as a UV-source and a photomask, which has four rectangular windows. The photomask is a glass substrate, with evaporated chromium patterns on top, which are opaque to UV-light. The photomask was fabricated with positive electron beam lithography, where cromium was wet etched away from exposured areas with a mixture of aqueous potassium ferricyanide and sodium hydroxide, using PMMA as the etching masks.

After exposure, the photoresist is developed (see Fig. 2.3 (a)) with AZ351B, which is NaOH based developer. Next, silicon nitride is removed from the developed areas by plasma etching in RIE (see Fig. 2.3 (b)). Gases used are CHF_3 (50.0 sccm) and O_2 (5.0 sccm), pressure 55 mTorr and RF-power 150 W, when the etching rate is $\sim$ 50 nm/min. Crystalline silicon is then wet etched in 30 % KOH at $\sim$ 95 °C for $\sim$ 5 h, after which, the chips are cleaned in hot, deionized water, and lastly, rinsed with isopropanol and dried with nitrogen gas. The cross section of a suspended silicon nitride membrane is shown in figure 2.3 (c).

It is also possible to thin the completed silicon nitride membrane to a desired thickness by plasma etching them afterwards from the front. The parameters for the etching process are the same as explained above. The rms surface roughness perpendicular to the plane of the membrane after the etching was determinated by atomic force microscope (AFM) and it is about 1-2 nm. The roughness does not increase during the thinning process, which indicates that the plasma etching is dominated by volatile reaction products, and not by sputtering.

2.3 Measurement setup

All experiments discussed in this thesis are performed with a home-made plastic He^3-He^4 dilution refrigerator (model PDR-50) reaching a base temperature of ~ 50 mK [7]. The refrigerator has ten measurement lines, which are filtered several ways. Eight of the lines are stainless steel coaxial cable type SS from room temperature to 4.2 K, where they are connected to RC-filters (R= 1 kΩ and C= 1 μF). From 4.2 K to sample stage the lines continues as Thermocoax cables, which filter the high frequencies [8]. Two of the lines are also stainless steel coaxial cable from room temperature to 4.2 K, but they continue as twisted pair of high resistance manganin wires to the sample stage, where are 1 kΩ resistors in series with manganin wires. These lines enables high frequency measurements.

Temperature of the sample stage is measured with a ruthenium oxide thermometer (RuO) from Lake Shore Cryotronics, whose resistance is read by a Picowatt AVS-47 resistance bridge. The thermometer was calibrated against a Germanium resistor, GR-200A-30, also from Lake Shore Cryotronics.

During the measurements, the refrigerator and measurement electronics are inside of a shielded room. Measured signals are amplified by room temperature Ithaco Low Noise (1201/1211) preamplifiers and the preamp output is read by a digital voltmeter (DVM) with a multiplexer input and transferred to the computer by an optical fiber to avoid electrical contact between the computer and the measurement electronics. The DVM is read through the GPIB channel by Labview software.

Chapter 3

Tunnel junction thermometry

Tunnel junctions are structures, where two metallic electrodes are separated by a thin insulation layer. The metallic electrodes can either be in the normal or in the superconducting state and the insulating layer is thin enough to allow quantum mechanical tunneling for electrons. Nowadays, tunnel junction are basic building blocks for many mesoscopic electronic devices [2], and in this thesis, symmetrical normal metal-insulator-superconductor tunnel junction pairs, known as SINIS structure, are used to measure temperature below 1 K.

In this chapter, the current-voltage (IV) characteristics of NIS tunnel junctions are first discussed in section 3.1. Thereafter, the operation of the SINIS tunnel junction thermometry is presented, and the limitations of the device are discussed in section 3.2.

3.1 IV characteristic of Normal metal - Insulator - Superconductor (NIS) tunnel junctions

An NIS structure consists of a normal metal electrode, a thin insulator layer and a superconducting electrode in series. The quantum mechanical tunneling phenomenon through this structure was first observed experimentally by Giaver in 1960 [9]. The theoretical single particle current for NIS structure can be calculated from the tunneling Hamiltonian [10] yielding a result for the current through the NIS junction

$$I(V,T) = \frac{1}{2eR_T}\int_{-\infty}^{\infty} n_s(E)\left[f_N(E-eV,T_{e,N}) - f_N(E+eV,T_{e,N})\right]dE, \tag{3.1}$$

where R_T is the tunneling resistance of the junction, $n_s(E) = N_s(E)/N_N(0) = |E|/\sqrt{E^2-\Delta^2}$ the density of states (DOS) of the weak coupling superconductor, f_N the Fermi-Dirac distribution and $T_{e,N}$ the electron temperature of the normal metal [10, 2]. We can immediately see from Eq. (3.1) an unexpected property of this structure: The current through it depends only on the electron temperature of the normal metal. The temperature of the superconductor affects only indirectly through the temperature dependence of Δ. In Eq. (3.1) also elastic tunneling is assumed .

At low temperatures ($k_B T \ll \Delta$) and voltages ($0 < V < \Delta/e$), the current has the following approximative form

$$I(V,T) \approx I_0 e^{\frac{eV-\Delta}{k_B T_{e,N}}}, \tag{3.2}$$

where the characteristic current for an NIS junction is $I_0 = \frac{\Delta}{eR_T\sqrt{\frac{\pi k_B Te,N}{2\Delta}}}$ [11]. Figure 3.1 (a) shows measured current-voltage curves of two NIS junctions in series, (SINIS structure), at various temperatures below 1 K, and figure 3.1 (b) the numerical derivative of the IV curve at the lowest temperature T=64 mK from which Δ and R_T can be experimentally determined. It is clear that the shape of the IV–curve indeed heavily depends on the temperature as can be seen also from Eq. (3.2). SINIS structures are nowadays widely used as sensitive, low temperature thermometers in nanostructures [11, 12, 2, 13, 14, III], partly because of their ability to probe the electron temperature of a structure directly.

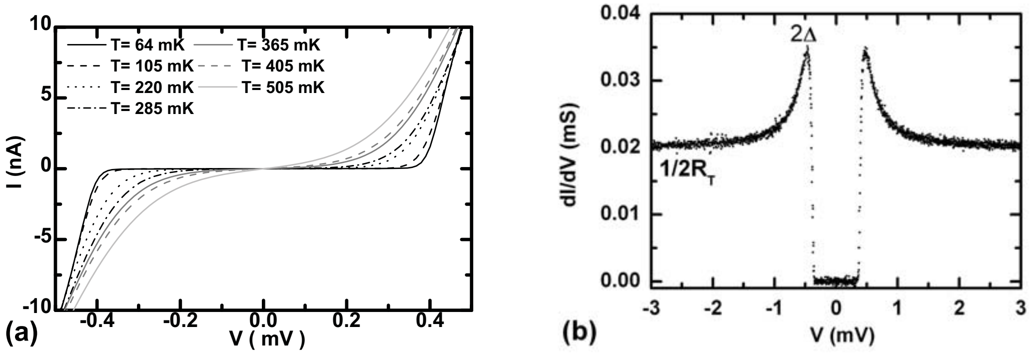

Figure 3.1 (a) Measured I–V characteristics of SINIS structure at various base temperatures. (b) Numerical derivative of the IV–curve in (a) measured at the lowest base temperature, T=64 mK. It is possible to define the tunneling resistance, R_T, and the energy gap, Δ, from the derivative as shown in the figure.

Another common application for a NIS structure at low temperatures is electron cooling [11, 2]. When the junction is biased below the energy gap, $V \leq \Delta/e$, electron tunneling from the normal metal to the superconductor can lower the temperature of the normal metal. It has been shown that it is possible to cool down even macroscopic objects with this technique at low temperatures [13].

3.2 SINIS tunnel junction thermometry

We have seen from eq. (3.2) and fig. 3.1 (a) that the IV– curve of SINIS structure depends strongly on temperature of the normal metal at low temperatures, and that this feature makes thermometric applications possible. A SINIS thermometer has also other advantages such as its small size, easy integrability to nano- and mesoscopic systems, low self-heating and high sensitivity, all of reasons which make it very attractive as a low temperature thermometer.

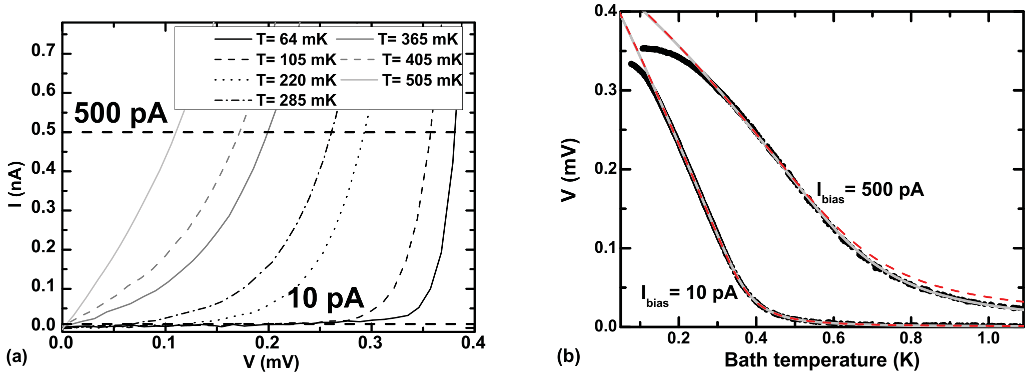

Figure 3.2 (a) An enlargement of a typical operational area of SINIS thermometer IV curves. The horizontal dashed lines are constant current bias at $I = 500$ pA and $I = 10$ pA.(b) Measured calibration curves (black circles) for SINIS with two different bias currents and the corresponding curves from BCS theory. Light gray: BCS theory with $\Delta(T)$, red dashed lines: with $\Delta(0)$.

In figure 3.2 (a) an enlargement to the operational area of SINIS tunnel junction thermometer on IV–characteristics is presented. SINIS can be used as a thermometer either by biasing the junction at a constant current or voltage and measuring the other variable as a function of temperature. Usually current bias is used, because then differential voltage amplifiers can be used in the measurement. This operation mode is depicted in fig. 3.2 (a), where the horizontal dashed lines represent two different constant current bias values typically used.

Measured calibration curves (black circles), $V(T)$, for SINIS thermometer with two different bias current values and the corresponding numerically calculated curves from Eq. (3.2) (light gray and red dashed lines) are shown in figure 3.2 (b). The calibration is performed by decreasing the bath temperature of the refrigerator, T_{Bath}, slowly to ensure the sample stage was in thermal equilibrium with a calibrated ruthenium oxide thermometer, and measuring simultaneously the voltage response of the SINIS. The theory curves are calculated without any fitting parameters (assuming that the NIS junctions are identical), because the energy gap, Δ, and the tunneling resistance, R_T, are determined independently from the IV-curves (3.1 (b)). The light gray line is calculated assuming that the energy gap is temperature dependent, which is the case during the calibration, whereas the dashed red lines keep Δ constant.

We can immediately see that at the lowest temperatures, the measured voltage start to deviate from the theoretical curve. This saturation has been seen to depend on the strength of the electron-phonon interaction, *i.e.* the size of the thermometer and the type of the substrate, the electrical impedance of the junction and filtering, hence the reason for the saturation in this work is external noise heating coming through the measurement leads. However, the saturation could also be caused by the broadening of the DOS, which is due to the finite lifetime of quasiparticles and depends on material quality [15,16,17], or higher order tunneling processes (the Andreev current) [18]. Usually broadening of the DOS is not a problem for evaporated Al films, because we can choose the bias current above the sub-gap current region, where its effects dominate. Also the higher order tunneling processes dominate only in large and more transparent junctions. On the other hand, if the junctions have a small enough capacitance, $E_C \gg k_B T$, charging effects can play a role and change the shape of calibration curve [19]. However for the junctions and the temperature range used in this work, this effect is minimal. In conclusion, to get the correct electron temperature in our experiments, the measured SINIS voltage must be converted to temperature by using the theory to correct the overheating effect.

However, depending on the sample geometry, during the measurement the superconducting leads of a SINIS can stay cold or warm up with the normal metal even though the base temperature of the refrigerator stays around 60 mK. If the leads are at the base temperature, the energy gap is fully open and the BCS conversion curve needs to be calculated assuming that $\Delta(T = 0K)$, which is the red, dashed line in figure 3.2 (b). On the other hand, if the leads warm up, the conversion curve must be calculated assuming that the energy gap is a function of temperature as it is during the calibration.

It is clear from figure 3.2 (b) that the calibration curve measured with a smaller bias, $I_{bias} = 10$ pA, has a stronger slope below 0.4 K, but less response at the higher temperatures, compared to the higher bias curve, $I_{bias} = 500$ pA. For the higher bias currents, the power dissipation in the normal metal due to the bias current is significantly larger, and due to this, the sensitivity in the lowest temperatures is lost. Thus by using a few different bias values, it is possible to measure the temperature in a large temperature range from 100 mK up to 1 K by using Al based junctions.

Finally, we will discuss the heat leak, *i.e.* the effect of cooling, through the biased SINIS junction. The cooling power of a NIS junction is calculated from [11]

$$P(V,T) = \frac{1}{e^2 R_T} \int\limits_0^\infty (E - eV) n_s(E) \left[f_N(E - eV, T_N) - f_N(E + eV, T_N) \right] dE. \tag{3.3}$$

In the limit of low temperatures, the bias voltage for maximum cooling is $V \lesssim \Delta/e$ and therefore the optimum cooling power has an approximate form [2]

$$P(V,T)_{opt.} \approx 0.6 \frac{\sqrt{\Delta}}{e^2 R_T} \left(k_B T_{e,N} \right)^{3/2}, \tag{3.4}$$

when $T_S \ll \Delta/k_B$. We can immediately see from equation (3.4) that the cooling power can be varied by changing the value of tunneling resistance R_T and the value of energy gap Δ. The tunneling resistance can be controlled by varying the size of the junction area and the thickness of the barrier, *i.e.* transparency, and the difference in R_T can be easily orders of magnitude. The value of Δ can be varied by changing the superconducting material or changing the film thickness [20,21]. For evaporated aluminum films, which is the most widely used material in tunnel junction applications, the increase of Δ has been reported to be up to 30 %, when film thickness is decreased from 30 nm to 5 nm [20], but the effect is still small compared to the variation of R_T.

Typically, the total tunneling resistance of the thermometer is $2R_T \sim$ 50 kΩ and $\Delta \sim$ 0.22 mV for thin aluminum films. By using these values in equation (3.4), the maximum cooling power in tunnel junction thermometer is $\sim$ 23 fW at 0.3 K. If the used bias point differs from the optimum, the cooling power decreases very rapidly.

Chapter 4

Theory of electron–phonon coupling

Electron-phonon (e–p) scattering is the dominant mechanism for electron energy relaxation below 1 K. It is an established fact that the coupling is weak enough to enable the situation, in which conduction electrons and the lattice are at significantly different temperatures. The strength of the electron-phonon coupling depends on several material parameters and also the dimensionality of the phonons.

In section 4.1, theory of electron-phonon scattering in the case of three dimensional phonons is presented including a discussion on the effect of disorder. Also results from previous experiments are briefly summarized. Finally, the influence of phonon dimensionality is discussed in section 4.2.

4.1 Electron–phonon coupling in the case of 3D phonons

In general, electron-phonon scattering rate has a form

$$\frac{1}{\tau_{e-p}} = \alpha T^m \tag{4.1}$$

and thus the corresponding net power transferred from hot electron to phonons is

$$P = \Sigma\Omega\left(T_e^n - T_p^n\right), \tag{4.2}$$

where Σ is the e–p coupling constant, Ω the volume of the heated part of the metal, T_e the electron and T_p the phonon temperature, and $n = m + 2$. The constant Σ and the value of exponent n depend on the parameter ql, in which q is the wave vector of the dominant thermal phonons and l the electron mean free path. If $ql \gg 1$, the sample is considered to be ordered, and if $ql \ll 1$, it is disordered with respect to e–p interaction.

In ordered metals at low temperatures, electrons scatter only from longitudinal, or from both longitudinal and transverse acoustical phonons depending on temperature and material [22]. In the scalar deformation potential model, electrons scatter only from longitudinal phonons, if a 3D electron gas with spherical Fermi surface and 3D acoustic phonons with a linear dispersion relation is assumed. This means that sample dimensions are much larger than the average phonon wavelength and that Umklapp process can be neglected [23]. In this case, the temperature dependence for the scattering rate in equation (4.1) is $m = 3$, and the coupling constant is a material dependent parameter [24,23]. If both longitudinal and transverse phonon modes interact with electrons, the situation is more complicated and the scattering rate has a form ($k_B = 1$ and $\hbar = 1$)

$$\frac{1}{\tau_{e-p}} = \frac{3\pi^2 \beta_t T^2}{(p_F u_t)(p_F l)} \frac{\tau}{\tilde{\tau}} + \frac{7\pi\zeta(3)\beta_l T^3}{2(p_F u_l)^2}, \tag{4.3}$$

where u_t and u_l are the transverse and longitudinal sound velocities, $\beta_t = \beta_l \left(\frac{u_l}{u_t}\right)^2 = \left(\frac{2\epsilon_F}{3}\right)^2 \frac{m p_F}{2\pi^2 \rho u_t^2}$, where ϵ_F is the Fermi energy, p_F the Fermi momentum and ρ mass density, and $\tau = l/v_F$ and $\tilde{\tau} = \tilde{l}/c_F$ the electron scattering times from vibrating and all (vibrating and stationary) impurities [25]. Here, the T^2 dependence arises from impurity mediated electron-transverse phonon scattering.

From equation (4.3), we can see that if transverse modes are dominant, the exponent for the temperature dependence of the scattering rate is $m = 2$ and the coupling constant Σ scales with the electron mean free path, *i.e.* $\Sigma \propto \frac{1}{l}$. However, if the scattering is equally intensive from both modes, the situation is more complex. The temperature dependence of τ_{e-p} can vary between $m = 2 - 3$ and the coupling constant $\Sigma \propto \frac{1}{l} - l^0$.

In disordered limit $ql \ll 1$, the scattering processes from impurities, defects and boundaries are important, e–p interaction needs to be described as a interference process between electron-phonon and electron-impurity scattering. Sergeev *et. al* [25] have developed a model, in which the scattering can happen either from vibrating or static impurities. Then the scattering rate has a form ($k_B = 1$ and $\hbar = 1$)

$$\frac{1}{\tau_{e-p}} = \frac{\pi^4 T^4}{5\hbar^2}(p_F l)\left(\frac{\beta_l}{(p_F u_l)^3} + \frac{3\beta_t}{2(p_F u_t)^3}\frac{\tau}{\tilde{\tau}}\right) + \frac{3\pi^2 T^2}{2 p_F l}\left(1 - \frac{\tau}{\tilde{\tau}}\right)\left(\frac{\beta_l}{p_F u_l} + \frac{2\beta_t}{p_F u_t}\frac{\tau}{\tilde{\tau}}\right). \tag{4.4}$$

If the scattering potential is fully vibrating, *i.e.* the impurities are fully moving with the phonon mode ($\frac{\tau}{\tilde{\tau}} = 1$), the temperature dependence of the scattering rate is $m = 4$ and $\Sigma \propto l$. However, when the scattering potential is static, i.e. $\frac{\tau}{\tilde{\tau}} = 0$, only longitudinal phonons contribute. In this case, $m = 2$ and $\Sigma \propto \frac{1}{l}$ in the low temperature limit. Between these two extremes, both scattering potentials affect the rate and the exponent of temperature dependence can vary from $m = 2 - 4$ and $\Sigma \propto \frac{1}{l} - l$, according to the theory.

In several earlier studies [26, 27, 23, 28, 29, 30, 31], $1/\tau \propto T^3$ dependence is observed, and hence the simplest theory in a clean limit is widely used to describe metallic thin film samples at low temperatures, even though some samples have been in a region of moderate or strong disorder. However, it is impossible to conclude reliably the scattering mechanism for electron-phonon coupling from the exponent of the temperature dependence alone. Thus, systematic study of both the coupling constant Σ and the temperature dependence is essential to have a full understanding, especially if $m \sim 3$. In the ordered case, also $1/\tau \propto T^2$ dependency has been observed in thick AuPd films [32]. In the limit of strong disorder, $1/\tau \propto T^6$ has been observed in Ti, Hf [33], Bi [34] and AlMn [35] films, in contrast $1/\tau \propto T^2$ was observed in titanium alloys (TiAl, TiSn, TiSnSc) [31], Au–doped indium oxide films [36] and ultrathin Au [37] films.

4.2 Electron–phonon coupling in the case of low dimensional phonons

Already the presence of a free surface drastically modifies the local phonon modes near the surface, within a depth $z < \lambda$, where λ is the characteristic bulk phonon wavelength [38]. Qu *et. al.* have calculated [39], how the free surface affects the electron–phonon coupling in the case of ordered thin film on the top of insulating substrate. They noticed that, firstly, the temperature exponent increases from the bulk value and, secondly, it is temperature dependent, $n(T)$. $n(T)$ is a nonmonotonic function and has a maximum nearby a cross-over temperature, $T^* = \frac{\hbar c_R}{k_B t}$, where c_R is the velocity of the Rayleigh surface wave and t the thickness of the metal film. At $T > T^*$ the exponent reaches the bulk value n =5. Below the cross-over temperature $T < T^*$, the modified surfaces modes penetrate more into the metal film reducing the strain, which is the reason for the changed electron-phonon coupling. The shape of $n(T)$ depends also on the thickness of the metal film so that, for example at 50 mK for 10 nm Cu film $n \sim$ 5.8 and for 100 nm Cu film $n \sim$ 5.7. In contrast at 1 K, $n \sim$ 5.1 and $n \sim$ 5 for the same thicknesses, respectively. Thus, a pure T^5 dependence should not be observed in thin metal films.

If the substrate has two stress-free boundaries, *i.e.* within a distance comparable to the dominant phonon wavelength, the 3D transversal and longitudinal bulk modes couple to each other forming a new set of eigenmodes: horizontal shear modes (*h*) and symmetric (*s*) and antisymmetric (*a*) Lamb modes [40]. The dispersion relation for the *h*–mode is $\omega = c_t\sqrt{k_{||}^2 + \left(\frac{m\pi}{d}\right)^2}$, where k is the wave vector component parallel to the membrane surface, d is the membrane thickness and $m = 0, 1, 2, ...$ the branch number. The Lamb modes are much more complicated than the shear modes and the dispersion relation can be only solved numerically.

In thin membranes, the three lowest branches are dominant at low temperatures, and they have analytical low frequency limits:

$$\begin{aligned} \omega_h &= c_t k_{||} \\ \omega_s &= c_s k_{||} \\ \omega_a &= \frac{\hbar}{2m} k_{||}^2, \end{aligned} \tag{4.5}$$

where $c_s = 2c_t\sqrt{\frac{c_l^2 - c_t^2}{c_l^2}}$ is the effective sound velocity of the *s*–mode and c_t and c_l are the sound velocities for the bulk transverse and longitudinal modes [41]. The lowest *a*–mode behaves like a particle with an effective mass $m^* = \hbar\left[2c_t d\sqrt{\frac{c_l^2 - c_t^2}{3c_l^2}}\right]^{-1}$, which means the particle–like behavior becomes stronger, when the membrane thickness decreases.

The lowest *a*–mode has a quadratic dispersion relation in the low frequency limit, which predicts nontrivial behavior for electron-phonon interaction in thin suspended membranes. However, this problem has gotten much less theoretical attention than the electron-phonon coupling in case of 3D bulk phonons, and detailed theory is not complete. Belitz *et. al.* [42] have calculated the electron– 2D phonon coupling in the temperature range 5-20 K, and according to them the temperature exponent of the scattering time is $m \sim$ 2.5. However, Johnson *et. al.* [43] used the horizontal shear and Lamb modes and the deformation potential model in their calculations and the dependence exponent is $m \sim$ 1.3 at low temperatures.

Chapter 5

Thermal gradients and electron–phonon coupling in non-uniformly heated mesoscopic wires below 1 K

Temperature is naturally the most critical quantity when thermal properties are studied, and its measurement becomes more and more difficult as temperature decreases. By Joule heating technique, we can easily create a situation, in which the conduction electrons and the lattice are at significantly different temperatures, an effect known as the hot-electron effect [26]. In this case, it is also possible to develop significant thermal gradients, if the heating is not uniform.

In this chapter, numerical and experimental results on temperature gradients in mesoscopic metallic wires below 1 K are presented. In a section 5.1 the model for the numerical simulations is introduced and the results from them are presented. In a section 5.2, the measurement scheme and experimental results are discussed, with a comparison to the numerical results. In section 5.2 we also discuss the results from electron–phonon coupling measurements.

5.1 Theoretical model

The temperature profile of a system depends on the ratio of heating and cooling as a function of position. In the case of non-uniform heating or cooling, it is possible to create thermal gradients into metallic wires at low temperatures. The magnitude of the effect depends on the electronic diffusion, *i.e.* electronic thermal conductivity, and the electron-phonon coupling. In 2D–wires, the heat flow can thus be modeled with the non-linear differential equation:

$$\frac{d}{dx}\left(\frac{\mathcal{L}}{\rho}T(x)\frac{dT(x)}{dx}\right) = \Sigma[T(x)^n - T_p^n] - \dot{q}_h(x) + \dot{q}_c(x), \tag{5.1}$$

where $\kappa = \mathcal{L}T/\rho$ is the Wiedemann-Franz law for the electronic thermal conductivity with $\mathcal{L} = \pi^2 k_B^2/(3e^2)$ the Lorentz number [44], Σ the electron-phonon coupling constant, n the exponent of the temperature dependence of the e–p coupling and T_p the phonon temperature. In equation (5.1), $\dot{q}_h(x)$ and $\dot{q}_c(x)$ are the power density profiles for heating and additional cooling. When heating is carried out with DC Joule heating, $\dot{q}_h(x) = \rho i^2 f(x)$, where ρ is resistivity and i DC current density. The function $f(x) = 1$, when $i \neq 0$, and $f(x) = 0$, when $i = 0$.

Our experimental geometry consists of a $\sim$ 500 μm long, thin normal metal wire, in which two superconducting leads are in direct contact to supply the DC heating current (see fig. 5.2). Because of Andreev reflection in the NS boundary, very little heat will escape from the normal metal wire through the superconducting leads [45,46,47] and the wire is uniformly Joule heated. In this case, the correct boundary conditions are the von Neumann type, where the heat flux at the end of the wire is zero. There is also a short, unheated stub (length $d \geq 9$ μm) in the wire, where electrons can diffuse and be cooled by phonons. Below 1 K, the typical electron-electron scattering length, $L_{e-e} \sim 1\mu$m, is much shorter than the length of the wire, which ensures a well-defined electron temperature in the wire. The wire is also long enough so that the effect of the multiple Andreev reflection can be neglected [48].

In figure 5.1 we show the calculated temperature profiles based on Eq. (5.1) for copper and aluminum manganese wires, which are heated with different Joule heating powers uniformly at position $x < 0$ and in which the unheated stub is at position $0 < x < 9$ μm. Material parameters used in the calculations are $\rho(Cu) = 2.5 \times 10^{-8}$, $\rho(AlMn) = 12.3 \times 10^{-8}$, $\Sigma(Cu) = 1.8 \times 10^9$ [W/K^{5}m^3] and $\Sigma(AlMn) = 3.4 \times 10^9$ [W/K^{6}m^3] determinated from measurements described in next section 5.2 with the phonon temperature set to the base temperature of the refrigerator, *i.e.* 60 mK. Firstly, it is clear that the short stub drastically affects the temperature profiles of the wires above 300 mK, even though the phononic energy relaxation length is much longer, from 10 μm to 1 mm, than the length of the stub below 1 K. Surprisingly, the effect is pronounced also in the area of uniform heating, x <0, which implies that the bulk electron temperature restricted only by e–p coupling can not be measured until at a distance $x > 40$ μm away from the stub end. Secondly, the effect is much stronger in AlMn, which is expected, if we compare the values of resistivity and the strength of e–p coupling in AlMn and Cu. AlMn has about five times higher resistivity and the measured electron-phonon coupling constant in AlMn sample

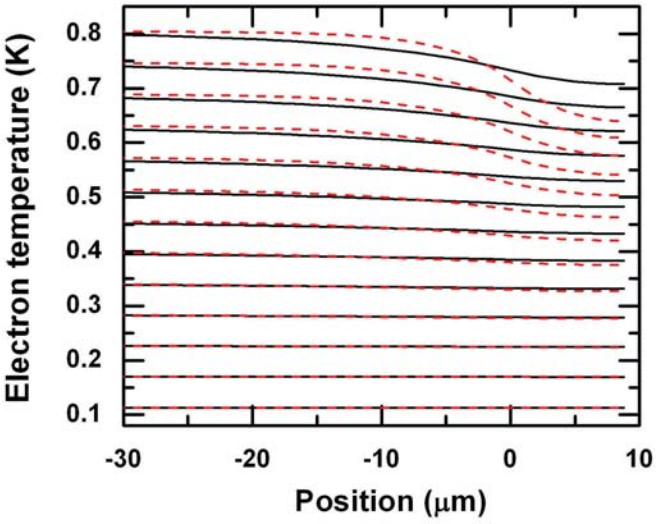

Figure 5.1 Calculated temperature profiles with different Joule power levels for Cu and AlMn wires. Solid (black) line uses material parameters for Cu sample and dashed (red) line for the AlMn sample.

is $\Sigma = 3.4 \times 10^9$ [W/K^{6}m^3] and for Cu sample $\Sigma = 1.8 \times 10^9$ [W/K^{5}m^3] and the exponent for the temperature dependency of the electron-phonon coupling is $n = 6$ and $n = 5$, respectively.

5.2 Measurement scheme and experimental results

The thermal gradients have been also investigated experimentally in several Cu and AlMn wires. Here the results for one Cu sample are presented and compared to the numerical results above. More results are shown in Ref. [II]. Samples are fabricated by using electron beam lithography and multi-angle evaporation techniques described in section 2.1 and the substrate has been oxidized or nitridized bulk silicon.

In figure 5.2 the schematic of the sample geometry and the measurement circuit is shown and in the table 5.1 the geometrical and material parameters of the sample determined by a scanning electron microscope (SEM) and an atomic force microscope (AFM). The hot-electron technique [26] is used to overheat the electrons above the lattice temperature in the experiment. All the samples have two normal metal wires, which are electrically isolated from each other. Two supercon-

Table 5.1 Parameters of measured Cu sample. L, d, d_1 and d_2 are defined in Fig. 5.2, t is the thickness, A the cross sectional area of the normal metal wire and ρ is the measured resistivity. ρ was determined from the IV measurement of the wire at the base temperature.

Sample	L [μm]	d [μm]	d_1 [μm]	d_2 [μm]	t [nm]	A [m^2]	ρ [Ωm]
Cu	473	11	3	8	48	1.5x10^{-14}	2.5x10^{-8}

ducting leads are directly connected to the longer Cu wire forming NS contacts and a slowly ramping DC voltage is applied across them to Joule heat the wire. The heating power $P = IV$ is measured in a four probe configuration simultaneously. Because of the Andreev reflection at the NS boundaries, the heating current is converted into a supercurrent in the superconductors and the Joule heat will not leak from the normal metal, when the NS-junctions are biased within the superconducting gap Δ [45, 46] and temperature is low enough to prevent the heat escape due to quasiparticle injection [49]. Hence, the NS contacts in a long wire do not create any thermal gradients to the normal metal, which means that the heating is uniform between the NS contacts and in the whole wire, the electron gas is cooled only by phonons, including the unheated stub [47]. Aluminum and niobium are usual choices for superconductors. Niobium has larger energy gap than aluminum, which means better thermal isolation, but on the other hand, it is difficult to fabricate a good quality niobium films by using conventional ebeam lithography and thermal evaporation.

The electron temperature is measured with a pair of oxidized aluminum (Al + AlO$_x$) leads forming a NIS tunnel junction pair, which are connected in the middle of the long Cu wire (the middle thermometer) and at the end, in the area of the unheated stub (the side thermometer). Detailed discussion of tunnel junction thermometry is already given in section 3.2, where we have argued that sizeable heat can not escape from the wire through the NIS junctions either. Therefore, the thermometer in the middle of the wire measures the temperature in a region without thermal gradients, and the electron temperature is defined by the dominant energy relaxation mechanism. At very low temperatures, the thermal resistance due to the electron-phonon interaction, R_{e-p}, overcomes the Kapitza boundary resistance, R_K, in thin metal films [26] and the electron energy relaxation is thus restricted by e–p coupling so that $p = \Sigma\left(T_e^n - T_p^n\right)$, where p is the heating power density. However, according to the numerical simulations presented above, the thermometer at the unheated stub is in the region of a gradient, therefore we should see a difference in temperature compared to the thermometer in the middle of the wire. It is also

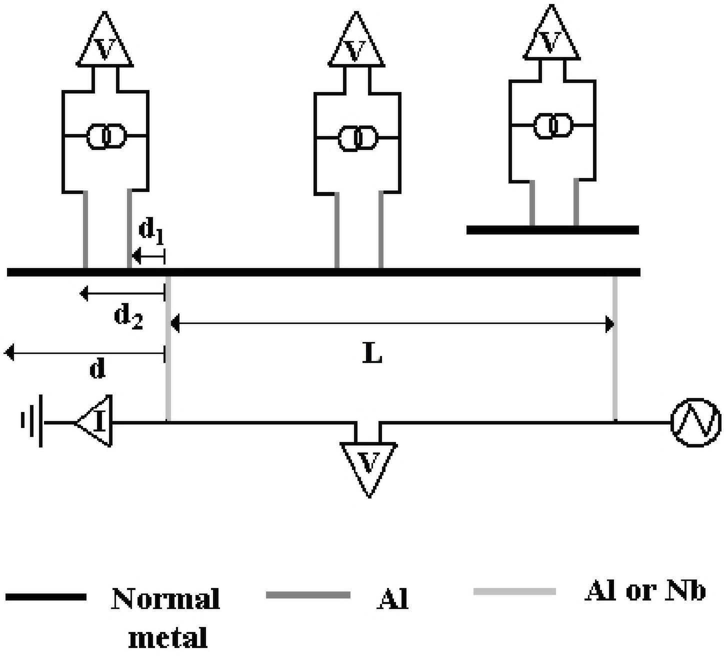

Figure 5.2 Schematic of the sample geometry and the measurement circuit. Black lines are the normal metal (Cu or AlMn), dark gray Al+AlO$_x$, and light gray Al or Nb. The Al+AlO$_x$ leads above the normal metal wire form NIS tunnel junctions, which are used to measure temperature. The Al or Nb leads below form NS contacts, which are used to apply the heating current. L is the length of the heated part of the wire and d is the length of the unheated stub. d_1 and d_2 are the positions of the NIS-junctions from the nearest NS-interface.

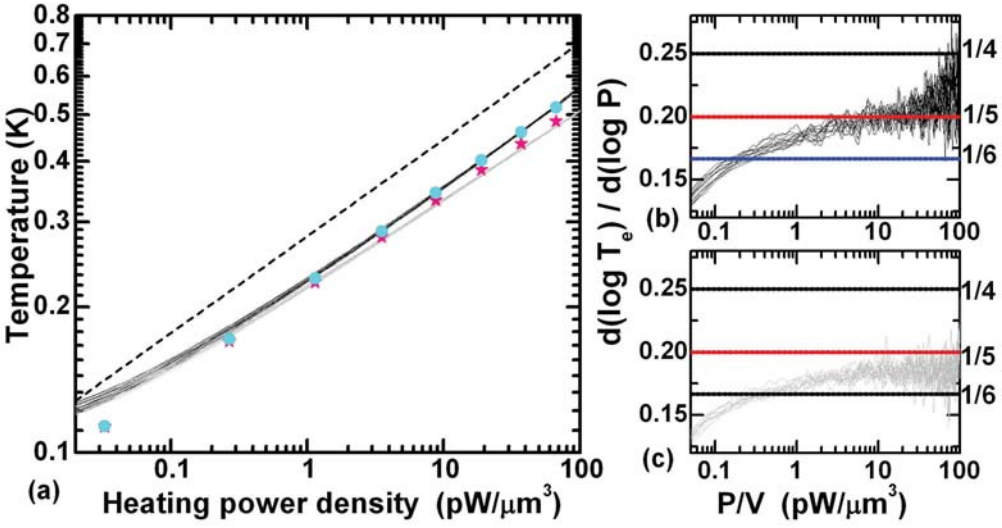

Figure 5.3 Data from Cu sample 1. (a) The temperatures of the thermometers versus heating power density in logarithmic scale. Black line: experimental data from the middle thermometer. Gray line: experimental data from the side thermometer. Cyan circles: numerical results for the middle thermometer, and pink stars: the numerical results for the side thermometer. Dashed line is a guide to the eye, $T \propto (P/V)^{1/5}$. The error bar for the temperature measured from the side thermometer is within the size of the data points. (b) and (c) The logarithmic numerical derivatives of the experimental data for the middle and the side thermometer, respectively.

important to notice that the SINIS thermometers here consist of two junctions separated by a small distance, ~ 5 μm, which means the junctions are at different temperatures, T_1 and T_2, in a region of the thermal gradient. Therefore, the temperature measured by the SINIS thermometer is in between these two temperatures, but it is not necessarily the average of T_1 and T_2, because of the non-linear character of the NIS thermometer. In the experiment, below the heated wire there is also an additional, short Cu wire with the SINIS thermometer (Fig. 5.2). This wire is thermalized to the lattice temperature and so that we can estimate the local phonon temperature, T_p.

Figure 5.3 (a) shows the measured temperature of the middle and the side thermometer versus applied heating power density P/V in logarithmic scale for Cu sample. We can immediately see that the thermometers are clearly at different temperatures, when $P/V \gg 1$ pW/μm^3, and at 100 pW/μm^3 the difference is already ~ 50 mK. The saturation of thermometers at the lowest temperatures is caused by noise heating, which is coming through measurement lines to thermometer. The theoretical results are calculated using the model in Eq. (5.1) with the appropriate sample parameters. Without a doubt the theory agrees well with the experimental data. This strongly implies that the temperature difference is indeed the consequence of electron diffusion and phonon cooling, as expected from the theory in the non-heated area of the wire.

We can study the exponent n of the electron-phonon coupling, if $T_e \gg T_p$. Then we can approximate that $P_{heat}/V = \Sigma T_e^n$ and calculate inverse of the exponent n from the logarithmic numerical derivative, $d(\log T_e)/d(\log P) = 1/n$. The phonon thermometer data is not shown here, but the approximation $T_e \gg T_p$ is valid for all the samples. In figure 5.3 (b) and (c) the inverse of the exponent n is plotted as a function of the heating power density P/V for the middle and side thermometer. For the middle thermometer, the exponent is ~5. However, the data from the side thermometer gives a higher exponent, ~ 5.5, and because of the thermal gradient this does not correspond to the power law of electron-phonon interaction. Similar results are also obtained from other Cu and AlMn samples [II].

Table 5.2 Measured values for electron mean free l path and coupling constant Σ of the Cu samples. t is the thickness of the metal film.

	Cu sample 1	Cu sample 2	Cu sample 3
t	48	32	28
l	27	22	17
Σ [W/K^{5}m^3]	1.8 $\times 10^9$	2.1 $\times 10^9$	2.5 $\times 10^9$

It is clear that the temperature of the middle thermometer is restricted by the electron-phonon coupling, which means that we can determine both the power law exponent and the coupling constant, Σ, from the data. We have measured three copper samples with different film thicknesses. The exponent of the power is for all the samples ~5, which is in agreement with previous results on Cu samples [26]. Using n =5 value, we can define Σ from the data. The results are presented in table 5.2 together with the calculated electron mean free paths based on resistivity. The coupling constant is clearly not only a material dependent parameter. On the contrary, it decreases when the electron mean free path increases, which implies increase of the sample purity. The conclusion is that the simplest theory for electron coupling, where Σ is a material parameter [23], does not apply in our samples. However, according to the more advanced theory for electron-phonon interaction, which was discussed in section 4.1, it is possible to have the exponent 5 for the power law and $\Sigma(l)$. In this case, the samples could be in the region of moderate disorder, where

$ql \sim 1$, or the scattering potential is not fully vibrating. In fact, the value of the parameter ql needs to be very close to zero before $n = 6$ is clearly observed.

Significant thermal gradients are surprisingly easy to create in mesoscopic samples below 1 K. This is a fact that needs to be considered, when thermal properties or thermometry are studied at low temperatures. The effect of thermal gradients extends even to the heated part of the sample as far as the e–p scattering length, L_{e-p}, which can vary from 1 mm to 10 μm as a function of temperature. We have also shown that electron–phonon coupling constant Σ is not only a material parameter as predicted by the simplest theory. On the contrary, the coupling constant is dependent on electron mean free path l, which is expected from the more advanced theory for electron–phonon coupling.

Chapter 6

The effect of phonon dimensionality on electron energy relaxation

During the last decades, electron-phonon coupling has been widely studied at low temperatures, but mostly the case, where samples are on bulk substrates, where coupling is mostly to three dimensional bulk phonons [26, 27, 23, 28, 29, 30, 31, 34, 33, 35,36]. However, an obvious question is, how does the phonon dimensionality affect the electron-phonon coupling? Nowadays, it is a standard procedure to fabricate suspended structures, in which the phonons form a quasi-2D or even a 1D system, and many devices and detector are usually placed in this kind of surroundings. Also according to theory [43, 42], phonon dimensionality should have a drastic effect on the electron-phonon interaction, but a clear experimental confirmation has not been reported before, even though a few attempts have been made [50, 51].

In this chapter, the experimental observations on the effect of phonon dimensionality on electron-phonon coupling below 1 K are presented. In section 6.1, the measurement scheme is described, and in section 6.2, the experimental results are presented. At the end of chapter 6.2, also the the effect of the Cu wire thickness on electron-phonon coupling in membrane and bulk samples is discussed.

6.1 Measurement scheme

The schematic of the sample and the measurement circuit are shown in figure 6.1. The idea of the measurement scheme is similar than in the study of thermal gradients and bulk e–p measurements presented in section 5.2. The long copper wire (L=500 μm) on top of a low stress silicon nitride membrane (size $\sim$600$\times$300 μm^2) is Joule heated by applying a slowly ramping DC voltage across the SN contacts, which are placed at the ends of the wire. The resulting electron temperature is

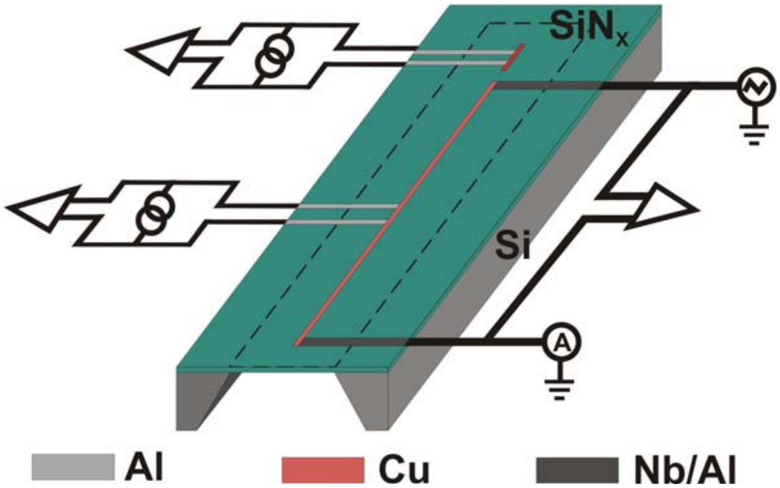

Figure 6.1 A schematic of the sample on a suspended membrane and the measurement circuit. Red lines are Cu, light gray $Al + AlO_x$ for SINIS junctions and dark gray Nb for SN contacts.

measured in the middle of the wire with a SINIS tunnel junction thermometer. At low temperatures, the electron-phonon coupling is the dominant energy relaxation mechanism for conduction electrons and hence, during the heating, electrons are driven to a higher temperature than the lattice. In this geometry, we do not have any unheated regions, which would create thermal gradients in the wire, and therefore T_e is fully defined by the condition $P_{heat} = P_{e-p}$, where $P_{heat} = IV$ and $P_{e-p} = \Sigma V \left(T_e^n - T_p^n\right)$. The short, electrically separated Cu wire is again used to estimate the local phonon temperature T_p.

We have measured several samples with identical metallic structures both on a membrane and on a bulk substrate to see clearly the effect of phonon dimensionality. The material parameters shown in table 6.1 are measured accurately by using an atomic force (AFM) and a scanning electron microscope (SEM). The electron mean free path is determinated from the dimensions of the samples and the resistance of the Cu wire, which is measured at base temperature 60 mK with a four probe configuration.

The heating measurements are done for 30, 200 and 750 nm thick membranes. According to the dimensionality crossover temperature [52]

$$T_{cr} = \frac{\hbar c_t}{2k_B d}, \tag{6.1}$$

where $c_t = 6200$ m/s is the velocity of transverse phonons for SiN$_x$ and d the total thickness, phonons in the thickest membrane are already in the 3D limit in the studied temperature range 0.1-1 K, but phonons in the thinnest membranes are in

Table 6.1 Parameters for the measured samples. M=suspended SiN_x membrane and B=bulk substrate. d is the thickness of the membrane, t the thickness of the Cu film, V volume of the heated Cu, l electron mean free path and τ the electron thermal relaxation time.

Sample	SiN_x d (nm)	Cu t (nm)	V $[(\mu\mathrm{m})^3]$	l (nm)	τ(0.2K) (μs)	τ(0.8K) (μs)
M1	30	14	2.71	5.7	2.6	0.16
B1	30	14	2.46	4.9	7.1	0.030
M2	200	14	2.44	4.6	15.0	0.11
B2	200	18	3.67	4.1	6.4	0.045
M3	30	19	5.50	11.2	2.2	0.30
B3	30	19	4.62	9.8	4.3	0.034
M4	750	22	6.09	10.3	3.1	0.030
B4	750	22	5.87	8.7	3.9	0.013
M5	30	32	6.09	22	1.8	0.31
B5	30	32	5.09	19	2.7	0.038
B6	SiO_x	32	7.10	22	1.6	0.031
M7	30	90	18.6	46	1.8	0.488
B7	30	90	19.1	46	1.9	0.066

the 2D limit below 0.5 K. Therefore, we should already observe the effect of phonon dimensionality by comparing the results from the thinnest and the thickest membranes sample.

6.2 Experimental results

The main results are shown in Fig. 6.2, in which the electron and phonon temperatures are plotted as a function of the applied heating power density, P/V, for all membrane samples with different thicknesses (M1:30, M2:200 and M4:750 nm thick membranes) and for a few representative bulk samples. The red dots represent the data from the thinnest membrane, M1, in which phonons are expected to be two dimensional below the estimated dimensionality crossover temperature $T_{cr} \sim 0.5$ K for M1. It is very clear that the thinnest membrane sample behaves differently than the other membrane samples or the corresponding bulk sample B1. At low heating powers, the temperature of M1 is surprisingly lower than in the other samples, which implies that the e-p coupling is stronger. At higher heating power, the T_e for M1 starts to increase more rapidly, an effect which is unclear at the moment.

The 200 nm thick membrane sample, M2 ($T_{cr} \sim 110$ mK), has the same power

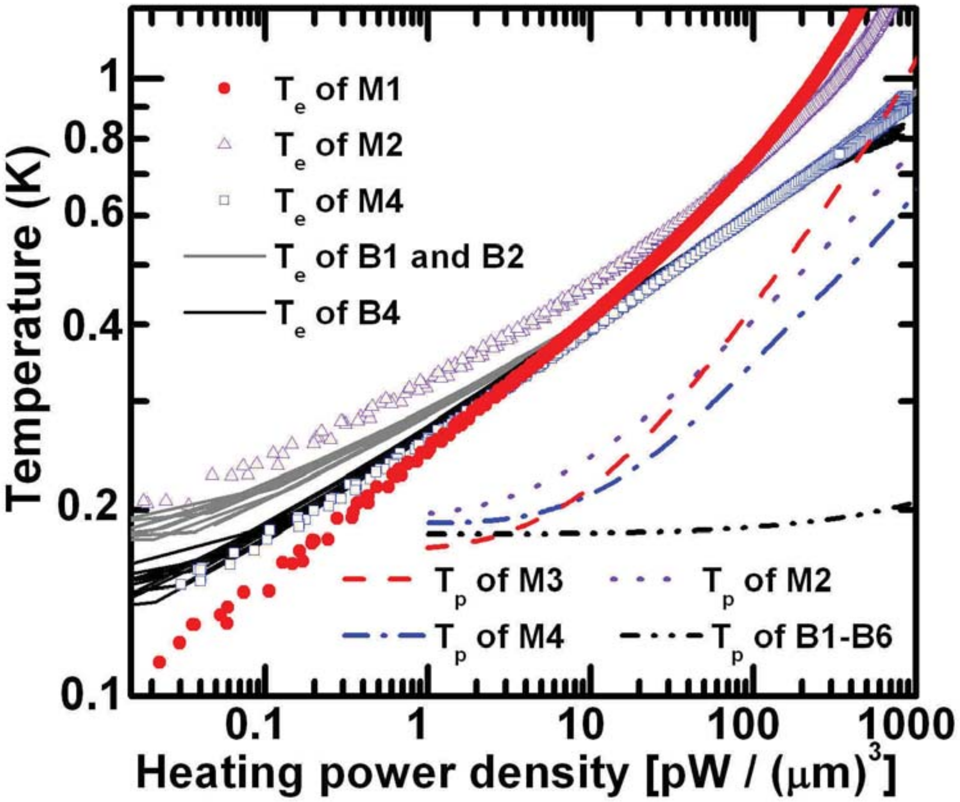

Figure 6.2 Measured electron and phonon temperatures T_e and T_p versus the applied heating power density P/V in log-log-scale. Red, solid dots: Te of sample M1 ($d = 30$ nm). Violet open triangles: T_e of sample M2 ($d = 200$ nm). Blue open squares:T_e of sample M4 ($d = 750$ nm). Gray line: T_e of samples B1 and B2. Black line: T_e of sample B4. Red dashed line: T_p of sample M3. Violet dotted line: T_p of M2. Blue dash-dotted line: T_p of M4. Black dash dot-dot line: T_p for all bulk samples.

law than the corresponding bulk sample, B2, even though the absolute value of temperature differs, which means that the nature of e–p coupling is weaker. At higher powers, the behavior of M2 is similar with M1. However, the 750 nm thick membrane sample, M4, behaves identically with its corresponding bulk sample, B4. This is reasonable, since $T_{cr} \sim 30$ mK for M4 implying that phonons are in the 3D limit in the studied temperature range.

The local phonon temperature increases much more rapidly in membranes than in the bulk samples, but the approximation $T_e^n \gg T_p^n$ is still valid in all the membrane samples, and we can measure the exponent n of the power law from the

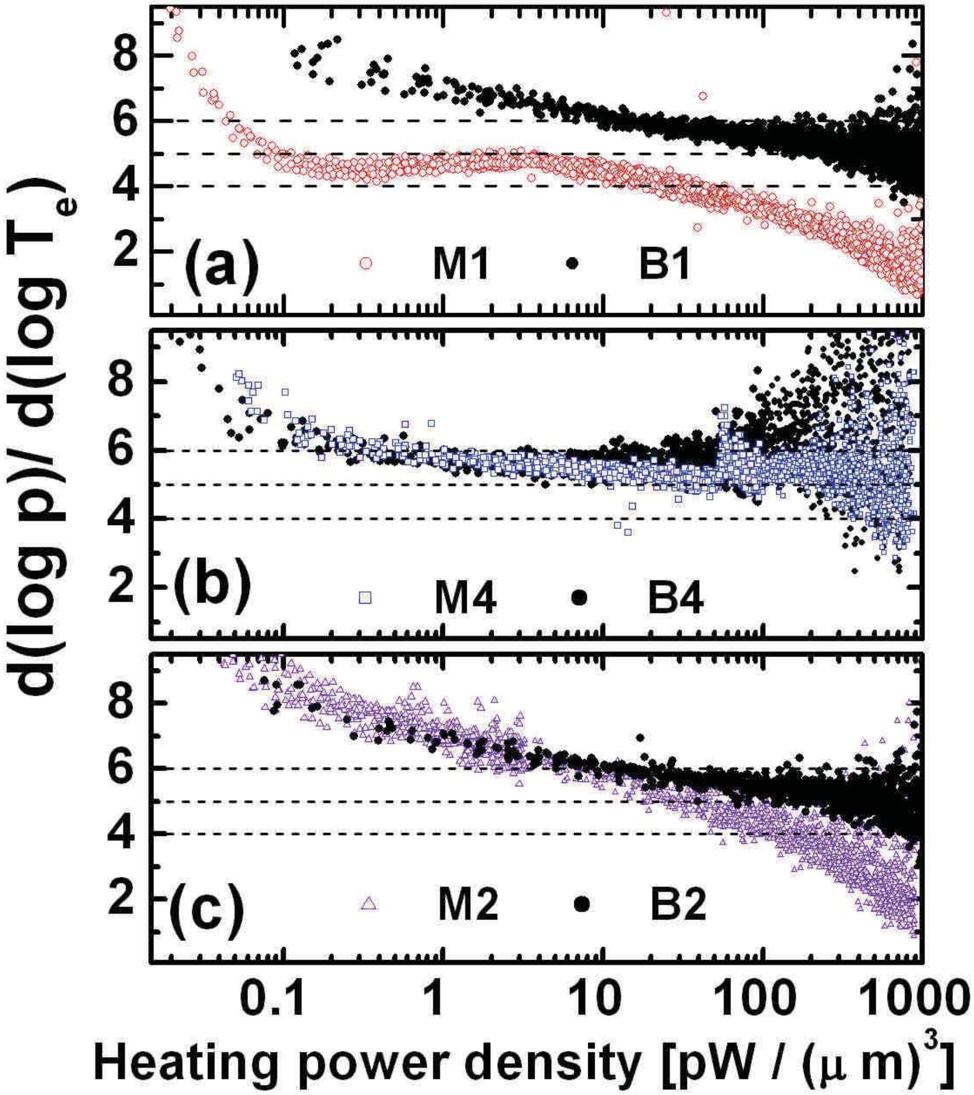

Figure 6.3 Numerical logarithmic derivatives of the data in Fig. 6.2 versus P/V for the membrane samples (a) M1 (d=30 nm), (b) M4 (d=750 nm) (c) M2 (d=200 nm) and for the corresponding bulk samples. Clearly, the temperature dependence of the thinnest membrane sample M1 differs from the corresponding bulk B1, or any other membrane sample.

numerical logarithmic derivative, as discussed in chapter 5. In figures 6.3 (a)-(c) the exponent n versus the applied heating power density is shown for each membrane and the corresponding bulk sample in the same graph. From Fig. 6.3 (a), we see that the temperature dependence of e–p coupling differs drastically between the 30 nm thick membrane M1 and the corresponding bulk sample B1. The measured exponent for the bulk sample B1 is $n \geq 6$ until the higher heating power densities, when n reaches the value $\sim$5. However, the membrane sample M1 have very clear plateau of $n \sim 4.5$. In contrast, the temperature dependence of the 200 nm and 750 nm membranes (M2 and M4) and the corresponding bulk samples (B2 and B4) are nearly identical with each other. The difference between samples B1, B2 and B4 is caused by the difference in thickness of Cu wire, which is discussed in more detailed below.

We have also studied the effect of the Cu wire thickness on e-p coupling in membrane and bulk samples. In figure 6.4 (a) the T_e versus P/V for four 30 nm thick membranes with a different Cu thickness from 14 to 90 nm is plotted and in figure 6.4 (b) the corresponding numerical logarithmic derivatives. Obviously, the absolute value of temperature does not depend on the film thickness in thin membrane samples at low heating powers, where e-p coupling is dominant. At higher heating powers, the thermal relaxation clearly weakens and depends on the thickness of the copper wire.

It is clear from Fig. 6.4 (c) that for bulk samples the strength of the electron-phonon interaction indeed depends on the Cu film thickness. The trend is that the thinner the Cu film, the higher the exponent n. This behavior is consistent with the theory, which takes into account the effect of the surface phonon modes [39], as discussed in section 4.2. Another reasonable explanation is that the amount of disorder increases in the samples as the film thickness decreases, which is also seen as the decreasing value of electron mean free path (Table 1). The disorders raises the value of n as the advanced theory of disordered 3D e-p coupling predicts [25]. Finally, the combination of these two theories can result in the observed behavior, but detailed theory is lacking. We have also observed the typically reported value of the exponent, $n =$5, in the sample B6, which is 32 nm thick Cu wire on top oxidized Si substrate. As the film thickness achieves the highest value 90 nm (sample B7), the clear plateau at $n \sim 4.5$ is observed. Either the Kapitza resistance becomes dominant, which is expected to happen at lower temperatures as the film thickness increases [53], or the sample is in the clean limit and electrons interact with both transverse and longitudinal phonons.

We can also compare the thermal relaxation times to see the effects described

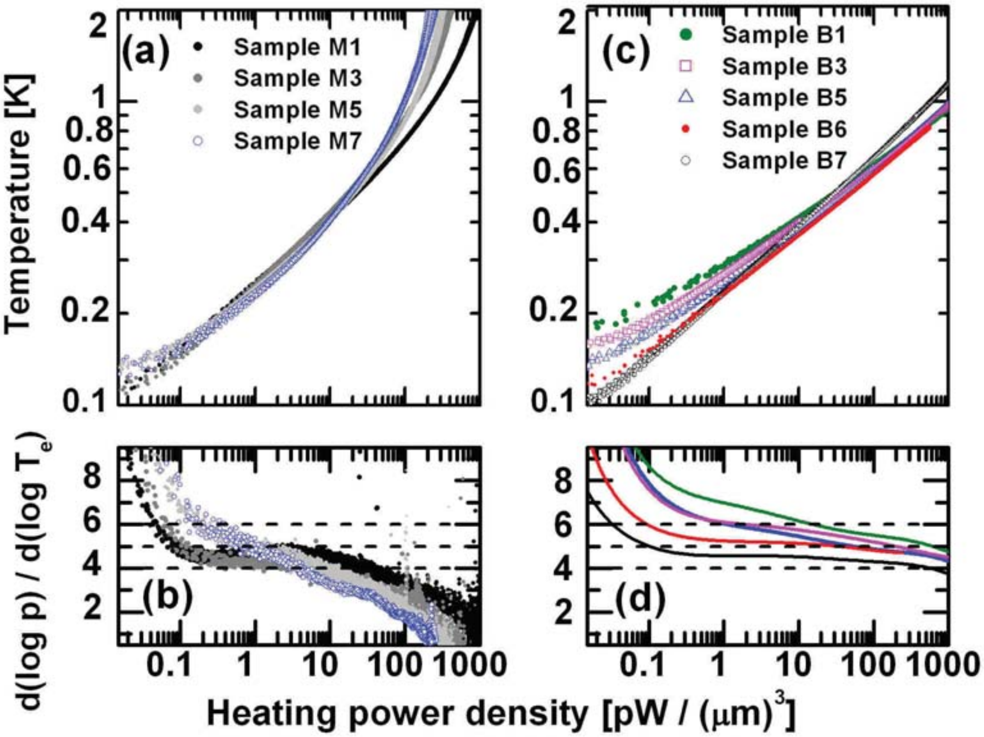

Figure 6.4 (a) T_e versus P/V for the thinnest membrane samples M1, M3. M5 and M7. (b) Numerical logarithmic derivatives of the data in Fig. (a). (c) T_e versus P/V for the corresponding bulk samples and the sample B6 on an oxidized Si substrate. (d) Numerical logarithmic derivatives of the data in (c). Noise has been filtered to help the eye. From top to bottom, Green line:B1, Magenta line: B3, Blue line:B5, Red line:B6 and Black line:B7.

above. The definition of the electron thermal relaxation time here is

$$\tau_e = R_{e-p} C_e = \frac{\gamma V T_e}{\frac{dP}{dT_e}} \sim \frac{\gamma T_e^2}{n \frac{P}{V}}, \tag{6.2}$$

where $R_{e-p}^{-1} = dP_{e-p}/dT_e = nV\Sigma T_e^{n-1}$ is the thermal resistance, $C_e = \gamma T_e V$ the heat capacity with the Sommerfeld constant $\gamma = 100$ J/K^{2}m^3 [54] and volume V. The τ_e is calculated at two different temperatures T_e=0.2 and 0.8 K for each sample, with the values presented in table 6.1. First of all, for the thinnest membranes, τ_e can be even three times shorter than in the corresponding bulk samples at $T = 0.2$ K. However, at higher temperatures the situation is reversed and the thermal relaxation is weaker in membrane samples. The general trend seems to be for both membrane and bulk samples that the scattering time decreases as the film thickness increases.

The strong difference between the 30 nm thick membrane and all the other samples is without a doubt due to the change in phonon dimensionality. The results presented here are the first experimental evidence that both the strength and the temperature dependence of the electron-phonon coupling significantly change as the phonon dimensionality is lowered. Surprisingly, e–p coupling becomes stronger as the 2D limit is reached. This implies that the lowest *a*–mode with quadratic dispersion relation plays an important role in the e–p coupling for 2D phonons. We have also observed possible evident for the effect of surface phonon modes in very thin Cu films on bulk substrates, which is not an established fact in the community.

Chapter 7

Phonon transport in suspended silicon nitride membranes below 1 K

The thermal properties of the surroundings are essential for optimizing the operation of many low temperature devices, but several fundamental phenomena are not yet deeply understood. Free–standing silicon nitride membranes are widely used structures in low temperature devices for example in detectors applications [4,2], because they enable easily efficient thermal isolation from the environment. However, understanding of thermal transport in SiN$_x$ membranes is still limited at low temperatures, although it has been studied by several authors [12, 55, 56, 57, 58]. For example, characterization of the phonon transport mechanism is not established, and heat transport has not yet been studied experimentally in low dimensional phonon systems at all.

In this chapter, unpublished results of phonon transport measurements for suspended SiN$_x$ membranes are presented for the case of 2D and 3D phonons over a temperature range 0.1 - 1 K. Phonon dimensionality is varied by changing the membrane thickness from 750 to 40 nm, which is known to span over the dimensionality crossover [III]. The membrane is heated with radially symmetric DC thin film heater, and the phonon temperature is measured at different distances from the heat source with the help of a SINIS tunnel junction thermometer. First, in section 7.1 the theory of phonon heat transport is briefly discussed, and previous experimental results are presented. In section 7.2, the optimized sample geometry, the measurement scheme and the data-analysis method for local phonon temperature are discussed, and finally, the experimental results are presented and discussed in section 7.3.

7.1 Background of phonon transport at low temperatures

Phonon transport in a system can be classified to be either ballistic or diffusive depending on the phonon's ability to scatter. When thermal transport is studied at low temperatures, the phonon mean free path defined by the internal scattering mechanisms (for example mass impurities, phonon-phonon scattering, two-level systems etc.) can become larger than the sample dimensions, therefore surface scattering starts to play an important role. This problem was already studied at 1938 by Casimir [59]. He suggested that the heat flow in a rod of a dielectric crystal can be described by a model, which is analogous to Planck's blackbody radiation theory and Stefan-Boltzmann radiation law. Consequently, in this phonon radiative transfer model, power flow has the form $P = A\sigma\xi T^4$, where A is the cross sectional area of the system perpendicular to the direction of heat flow, $\sigma = \pi^5 k_B^4/(15h^3)\sum_i 1/c_i^2$ is the Stefan-Boltzmann constant for phonons, where the summing is done over the three independent 3D bulk phonon modes with c_i speed of sound, and ξ is a constant, which describes the transport efficiency [59, 60, 61]. In this case, the surface roughness defines if the scattering is diffusive or specular. When phonons scatter specularly, *i.e.* the phase of the wave does not change, the phonon transport is ballistic and $\xi = 1$, which leads to the maximum value of thermal conductance. If the scattering is diffusive, which means that the phase is randomized in the scattering process, a sample is in the diffusive Casimir limit. In the Casimir limit, the effective boundary mean free path, which contributes in ξ, is defined in a following way:

$$l_{Casimir} = \frac{3}{4\pi S_c}\int\int |\mathbf{r} - \mathbf{r_B}| \cos\theta d\Omega dS_c, \tag{7.1}$$

where $|\mathbf{r} - \mathbf{r_B}|$ is the distance between a point $\mathbf{r}$ and a surface point $\mathbf{r_B}$, θ angle between $\mathbf{r} - \mathbf{r_B}$ and ∇T and S_c is the cross sectional area. The exact value of $l_{Casimir}$ depends on the geometry of the studied system and is temperature independent. For example $l_{Casimir}$=1.12$\sqrt{A}$ for a long square rod of cross section A and $l_{Casimir}$=2R for a long circular rod of radius R [59, 60].

However, if one or more of the dimensions of the system are of the order of the dominant phonon wavelength, the bulk phonon modes couple to each other and form a new set of eigenmodes as discussed in section 4.2. This will also affect phonon thermal transport. If an arbitrarily shaped heater with a circumference l is placed on top a thin membrane and the 3D phonon transport is ballistic, the radiated power has a form [52,62]

$$P_{3D} = \frac{2ld\pi^5}{15h^3}\left(\frac{2}{c_t^2}+\frac{1}{c_l^2}\right)\left(\frac{k_BT}{\hbar}\right)^4, \tag{7.2}$$

where d is the thickness of the membrane, c_t and c_l are speeds of sound for transverse and longitudinal phonon modes. In equation (7.2), it is assumed that the electrons are in thermal equilibrium with phonons and the Kapitza boundary resistance is neglected. The result is $P \propto dT^4$ as expected from the the phonon radiative transfer model discussed above. If we continue thinning the membrane or lower the temperature further, phonons reach the 2D limit ($Td \ll \hbar c_t/2k_B$) and the radiated power has a form [52,62]

$$P_{2D} = \frac{l\hbar}{2\pi^2}\left[\left(\frac{1}{c_t^2}+\frac{1}{c_l^2}\right)\Gamma(3)\zeta(3)\left(\frac{k_BT}{\hbar}\right)^3+\sqrt{\frac{2m^*}{\hbar}}\Gamma\left(\frac{5}{2}\right)\zeta\left(\frac{5}{2}\right)\left(\frac{k_BT}{\hbar}\right)^{5/2}\right], \tag{7.3}$$

where m^* the effective mass of the a mode. In the low temperature limit, the latter term starts to dominate and $P_{2D} \propto \frac{1}{\sqrt{d}}T^{5/2}$, because the effective mass depends on the membrane thickness.

If the membrane thickness d is decreased starting from the 3D limit at a constant temperature, first the thermal conductivity decreases. However, approximately at the dimensionality crossover thickness, $d_c = \hbar c_t/(2k_BT)$, the thermal conductivity reaches its minimum and starts to strongly increase again. The reason for this is that in 2D limit the effective mass m^* of the a–mode depends on d and $P \propto 1/\sqrt{d}$ [62]. This is also true in the diffusive boundary scattering case [63]. Hence due to the dimensionality crossover, very thin membranes are actually more effective thermal conductors than thicker ones, which has not yet been confirmed experimentally. For example for SiN$_x$ (c_t=6200 m/s) the critical membrane thickness is d_c =236 nm at 0.1 K and d_c =118 nm at 0.2 K, which are reasonable membrane thicknesses to fabricate.

One possible scattering mechanism in thin silicon nitride membranes for phonons are dynamic defects, known as two-level systems (TLSs) , which are formed from the amorphous structure of the membranes [64,65]. TLS is an atom or atoms, which can tunnel between two minima in configuration space. The tunneling can happen due to a deformation disturbance in the lattice. For example, a passing phonon can create such a perturbation and interact by scattering from a TLS, which decreases the thermal conductivity. In amorphous solids, the linear specific heat $c_V \propto T$ and the quadratic thermal conductivity $\kappa \propto T^2$, are explained by TLSes [64]. In amorphous 2D membranes, heat conductivity was calculated to have the form $\kappa \propto T(a + b\ln T)$ [65] in the low temperature limit, where only the lowest branch of each polarization is populated. However, in this case κ does not depend on m^* and thus if TLSs are the dominant scatterers for phonons, a minimum for κ is not observed at the dimensionality crossover thickness.

In previous experiments, Leivo *et. al* [12] studied phonon transport in 200 nm thick SiN$_x$ membranes, size 400×400 μm^2, by using two SINIS tunnel junctions as a heater and a thermometer. They reported that the temperature dependence is approximately $P \propto T^3$ below 1 K, and the data analysis was performed based on a diffusive model. They also restricted the thermal conductivity of the system by cutting the suspended bridges to the membrane and in this case $P \propto T^{2.5}$ was measured. Also Zink *et. al* [58] measured the heat transport in $\sim$ 200 nm membranes from 3-300 K with a large isothermal platform on top. Below 20 K they concluded that the heat transport is dominated by the surface scattering, but the detailed characterization was lacking.

Thermal conductivity has been also studied in thicker, 0.8-1.5 μm, SiN$_x$ membranes by several authors [55, 56, 57], but the conclusions have been inconsistent. Holmes *et. al* [55] measured phonon transport in several membranes with a large isothermal circular shape (R =100 μm) platform on top and varied the thickness of SiN$_x$ from 0.79 μm to 1.02 μm. Temperature was measured with a neutron transmutation doped (NTD) Ge resistor. They reported temperature dependences $P \propto T^{3.3}$ and $P \propto T^{3.2}$ for the thinner and thicker membranes respectively, over the temperature range from 0.1 K to 6 K. At the lowest temperatures $\sim$ 0.1 K, the absolute value of the thermal conductivity approached the fully ballistic limit, as analysed from the phonon radiative transfer model described above. The diffusive Casimir limit was analysed by using the value of the effective boundary mean free path for a rod with cross sectional area $A = L \times nL$ [66]. They also studied, how the surface conditions affect the thermal conductivity. They added Ag particles of diameter 100 nm and density 10 particles/μm^2 on the surface of the membrane and fabricated spokes of width and separation $\sim$ 5 μm by etching the membranes. In both cases the absolute value of the heat conductance was weakened, and the ballistic limit was not reached at the lowest temperatures. However, the temperature dependence did not change in the membrane with spokes compared to the bare membrane, but the change was clear in a case of Ag particles. Woodcraft *et. al* [57] studied the heat transport in 1.5 μm thick SiN$_x$ membranes of size 12.25×12.25 mm^2 with an isothermal Au platform of size 11×11 mm^2 on top connected to a NTD Ge thermometer. They observed that the data differed significantly from the ballistic limit analysed from the phonon radiative transfer model over temperature range 0.1 - 0.3 K and concluding that the heat transport was limited by the diffusive surface scattering. The reported temperature dependence was $P \propto T^3$. Furthermore Hoevers *et. al* [56] measured the heat transport in 1 μm thick SiN$_x$ membranes by using a superconducting to normal phase transition edge sensor (TES). The length of the membrane was 1.3 mm and the width was varied from 140 to 210 μm. They observed that at $T \approx 0.1$ K the transport is nearly ballistic ($\xi \approx 0.78 \pm 0.18$) by using the phonon radiative transfer model with a temperature dependence $P \propto T^{3.6}$. However the effective boundary mean free path used in the diffusive Casimir limit analysis was the one for a square rod $l_{Casimir} = 1.12\sqrt{A}$, incorrect for membranes.

The surprising conclusion from the results of the previous experiments is that pure $P \propto T^4$ dependence predicted by the theory in 3D limit is not observed in thick suspended SiN$_x$ membranes. The value of the exponent n is systematically lower. This indicates that the radiative model does not explain the experimental observations exhaustively, and an unknown scattering mechanism is contributing to the heat transport partly or dominantly. The previous experimental studies are also concentrated on thicker membranes, in which phonons are in the 3D limit, and no attempts to reach the 2D limit have been reported.

7.2 Measurement scheme and data-analysis method for phonon temperature

The idea of our measurement scheme is that a circular copper thin film heater (radius R_h =7 μm, width $w \sim$ 200-400 nm, thickness t=30 nm and perimeter 42.5 μm) with superconducting niobium leads (width $w \sim 1$ μm and thickness t =40 nm) in direct contact at both ends of the circle, is placed at the center of a suspended silicon nitride membrane. The fabrication methods for suspended SiN$_x$ membranes and metallic structures are explained in general level in chapter 2. The DC Joule heating technique described in chapter 5 is used to Joule heat the copper wire uniformly, which causes radially symmetric phonon emission power to the membrane. Simultaneously one or several SINIS (Al/AlO$_x$/Cu) tunnel junction thermometers (dimensions for the normal metal in SINIS: length $L = 14$ μm, width $w \sim$ 500-700 nm and thickness t=30 nm), which are described in chapter 3, are located on top the membrane at different distances from the center of the heater, to measure the local phonon temperature of the membrane during the heating.

The first obstacle was to find the optimized sample geometry. Figure 7.1 (a) and (b) show schematics of the two studied sample geometries. The more complicated geometry (called geometry 1) in Fig. 7.1 (a) contains eight tunnel junction thermometers at different distances from the center. The tunnel junction leads are oxidized aluminum and copper expect very nearby the junction area, where there is

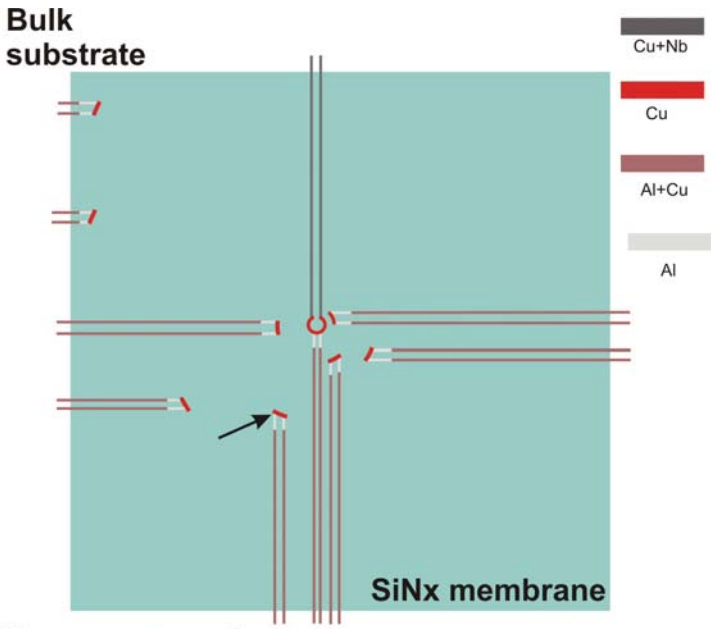

(a) Geometry 1

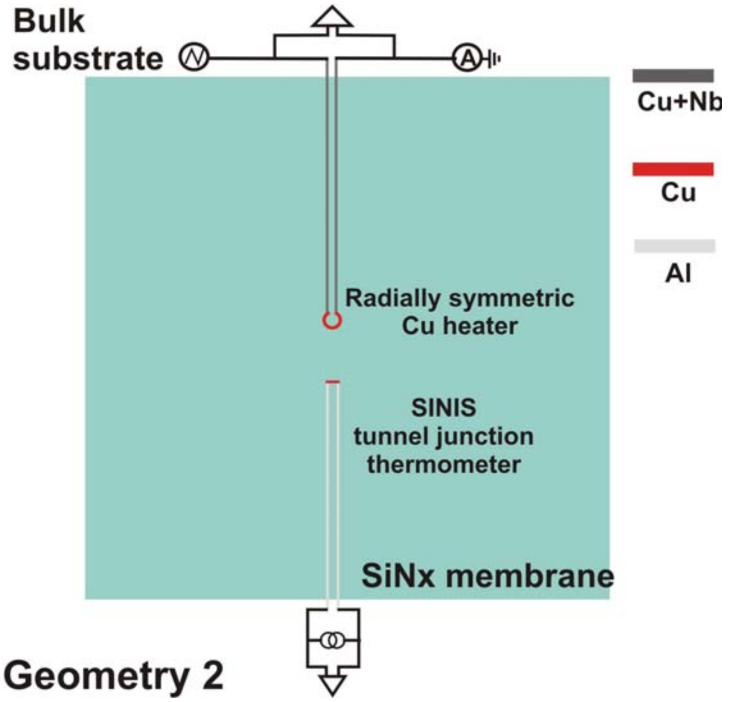

(b) Geometry 2

Figure 7.1 Schematics of the studied sample geometries and the measurement circuits. Light green area is a suspended SiN$_x$ membrane. (a) Geometry 1: eight phonon thermometers are placed from 15 μm to 250 μm away from the center. The thermometer leads are Al+AlO$_x$+Cu expect in the junction area and the arrow points to a SINIS thermometer, which is $\sim$100 μm away from the center of the heater. The measurement circuit is identical with the circuit presented in geometry 2. (b) Geometry 2: only one tunnel junction thermometer is at a time and the thermometer leads are only Al+AlO$_x$ on membrane. The heating power $P = IV$ is measured in a four probe configuration and SINIS tunnel junction thermometers are current biased.

only Al and AlO$_x$. All metallic structures are fabricated at the same time as described in section 2.1. In the simple geometry (called geometry 2) shown in Fig. 7.1 (b), only one thermometer is placed at a time on a membrane at varying distances from the heater, and the superconducting leads are bare aluminum with a thin oxidized layer on top. Due to the geometry, metallic structures are fabricated during two lithography cycles. During the first cycle, the tunnel junction is fabricated as described in section 2.1. In the next cycle, the heater is fabricated using only one thick (~ 1 μm) layer of PMMA baked at ~ 100 °C for 1 min, because copper will be damaged, if it is in contact to copolymer and in higher baking temperatures. The hypothesis is that in geometry 1 the large number of tunnel junction leads with copper affect the temperature profile of the membrane, since the normal metal absorbs and the leads can scatter the phonons creating an extra channel for the heat transport from the membrane. This effect can have a different impact to a measured temperature profile, depending on the strength of the electron-phonon coupling in a system. If the electron-phonon coupling is weak, the phonon emission is rare and the electron can diffuse out of the membrane through the leads after the absorption of a phonon. In this case, the temperature is expected to be lower in membrane with geometry 1. However, if the electron-phonon coupling is strong, the temperature is expected to be higher in geometry 1, because the electron in copper can re–emit the absorbed phonon.

Before we can discuss the measured data, the analysis method for the phonon temperature needs to be defined. In chapter 3.2 the saturation of a SINIS thermometer at low temperatures has been discussed with the conclusion that it is caused by noise heating power coming through measurement lines. This heats up the electrons above the lattice due to weak thermal coupling between these systems ($R_{thermal} = R_{e-p} + R_{Kapitza}$ and $R_{e-p} \gg R_{Kapitza}$ at low temperatures for thin films). Therefore the correct way to analyse the electron temperature, T_e, in the normal metal of the SINIS thermometer in the saturation area is to use the TV- curve calculated from the BCS theory instead the measured calibration curve.

However, in this experiment we are interested in phonon temperature of the substrate. At temperatures, where the measured and theoretical TV- curves collapse (see Fig. 7.2 (a)), the phonon and electron temperature are both equal to the cryostat temperature and T_p is measured correctly. However, in the saturation area the main question is, how much can the noise heating power, which is estimated to be $P_{noise} \ll 1$ pW, elevate the local phonon temperature on the membrane? It is an established fact that the electron-phonon coupling is very weak below 1 K [24, 26] and in the metal electrons and phonons are brought at different temperatures. If we make the well justified assumption that the local T_p is not rising appreciably due to

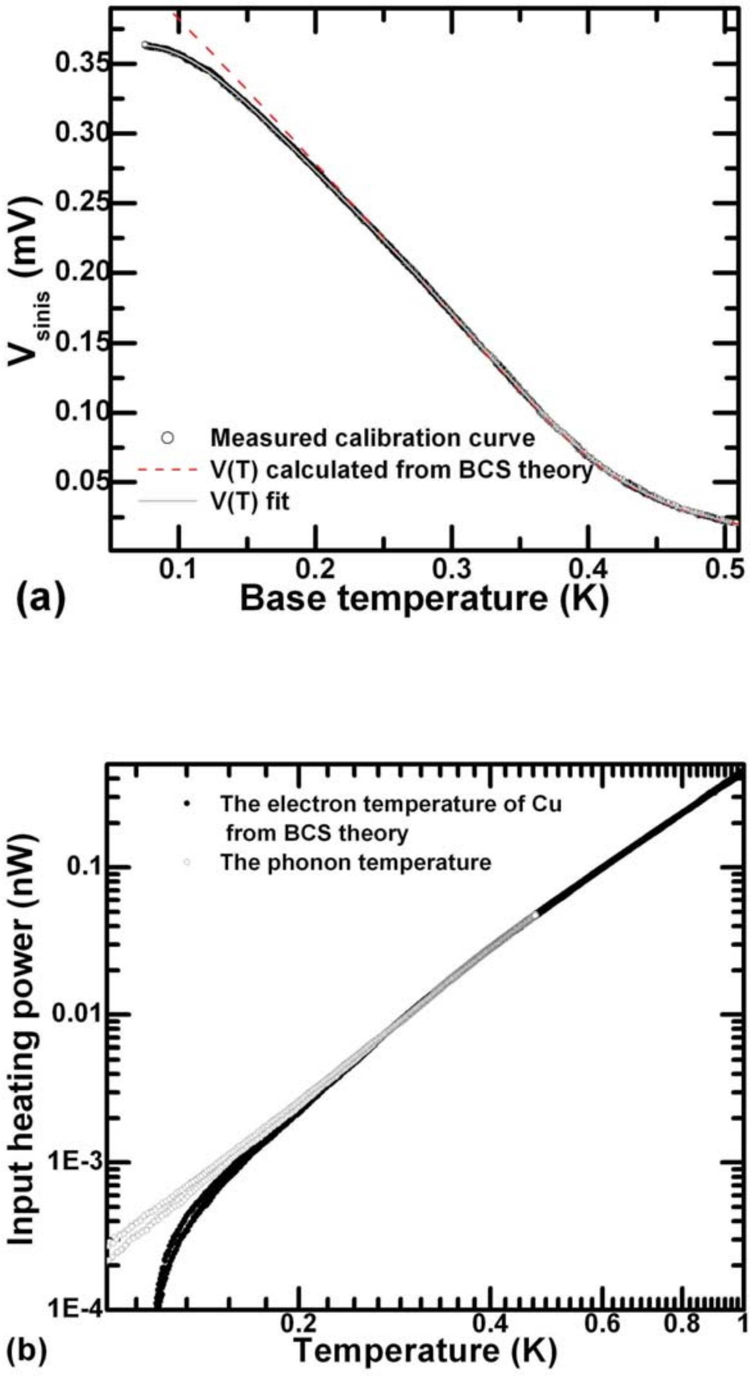

Figure 7.2 (a) A measured calibration curve for a SINIS (black, open circles), the corresponding curve for electron temperature from BCS theory (red dashed line) and $V(T)$ fit (grey line). (b) Input heating power P versus temperature T. Black dots: the electron temperature in Cu analysed by using BCS theory. Grey open circles: phonon temperature directly from measured $V(T)$- curve.

the noise heating power, *i.e.* $T_e \neq T_p = T_{cryostat}$, phonon temperature can be determinated directly from the measured calibration curve, in which the voltage across the thermometer correspond the measured cryostat temperature everywhere (see Fig. 7.2 (a) grey line) in the whole temperature range studied.

In Fig. 7.2 (b) the measured input heating power P versus temperature T is shown in logarithmic scale from the heating experiments performed for a sample with geometry 2 on top a 40 nm thick membrane, in which the distance between the thermometer and the center is 14.5 μm (sample M40b in table 7.1). The data is analysed in two different way described above. The black dots are the electron temperature of the Cu in SINIS thermometer analysed from BCS-theory and the grey, open circles the phonon temperature determinated directly from the measured calibration curve. The deviation of these two curve starts at 200 mK, when the electron temperature starts to saturate, but the phonon temperature continues clearly with the same slope. At 100 mK the temperature difference is $\sim$ 25 mK. The difference is not large in absolute values, but below 200 mK, the slope of the electron temperature curve is strongly affected by saturation, and does not correspond to the temperature dependence of the phonon transport. Therefore, in this work the data is analysed by using the measured calibration curve over the whole studied temperature range, but the results are plotted by dots in the area, where $T_e = T_p = T_{cryostat}$, and with open circles in the saturation area.

In figure 7.3 we compare the measured temperature response of heating experiments performed for the samples with geometry 1 and 2 on top of 200 nm thick membranes. In both samples, the distance between the studied thermometer and the center of the heater is $\sim$ 100 μm, which means in the geometry 1 the thermometer pointed by an arrow (see Fig. 7.1 (a)). Below 0.2 K, the temperatures are almost the same in both samples, but at higher temperatures they starts to differ, reaching a maximum difference $\Delta T = 141$ mK at $T \sim 0.8 - 0.9$ K. Because the temperature is lower in geometry 1, the leads apparently creates a channel for heat propagation out of the membrane. The effect seems to influence surprisingly strongly the shape of P versus T curve, which can be seen from the continues bending of the data of geometry 1 in Fig 7.3. The results are similar, but the maximum temperature difference is slightly smaller, when the thermometers are nearer, 40 μm away from the center (in geometry 1 the second thermometer from right). We have also compared the effect of geometry for 750 nm thick membranes for the same thermometer distances and surprisingly the effect is similar, but opposite. Temperature in samples made with geometry 1 is larger compared to samples made with geometry 2. This means that the electron-phonon coupling is much stronger in 750 nm than 200 nm thick membranes and a conclusion that was also confirmed in chapter 6.2 [III]. It is

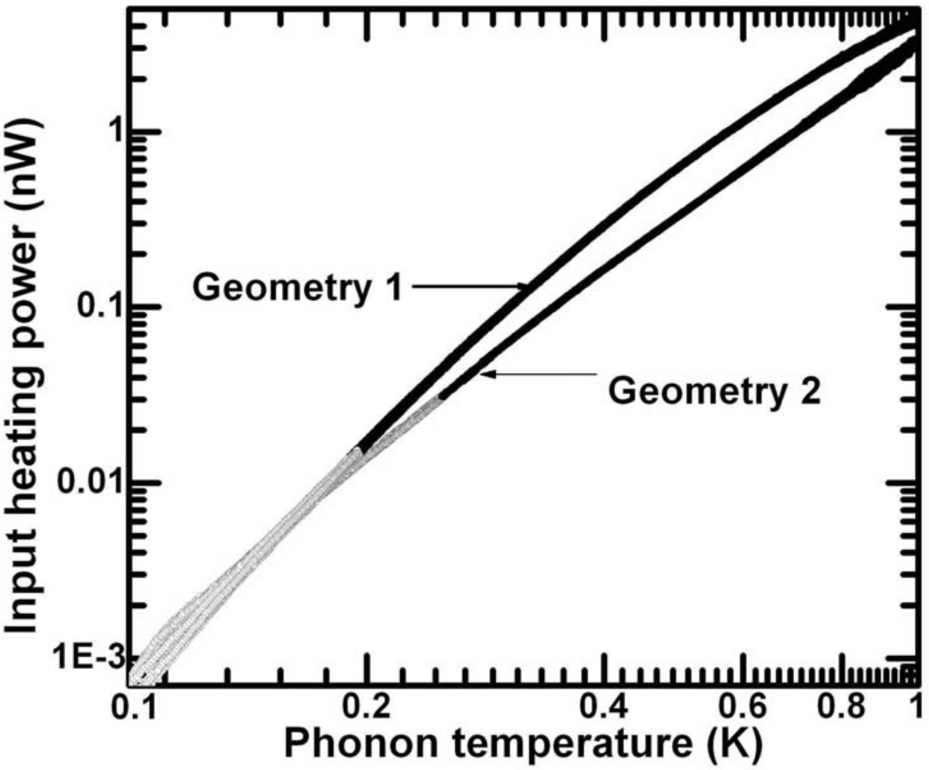

Figure 7.3 Measured input heating power P versus local phonon temperature T_p for samples with geometry 1 and 2, distance from heater center 100 μm. Black dots: temperature area where $T_e = T_p = T_{cryostat}$. Grey, open circle: temperature area, where $T_e \neq T_p = T_{cryostat}$. The maximum temperature difference between the two thermometers is ΔT_{max} =141 mK at $T \sim 0.8 - 0.9$ K.

clear that the extra leads affect strongly both the absolute value of temperature and the temperature dependence, as expected, and to minimize the effect of geometry, geometry 2 is the correct way to study phonon transport in SiN_x membranes.

7.3 Experimental results

We have studied altogether 29 samples and the results from 14 samples are presented in this chapter. In table 7.1 the important parameters for the studied samples are shown. For the thinnest membranes, which are $\sim$ 40 nm thick, geometry 2 is used for all samples, *i.e.* only one phonon thermometer at the time on the membrane, to avoid the creation of the excess propagation channel for heat. For samples on top of 200 nm thick membrane, a slightly modified geometry was tested and compared to the results measured from sample with geometry 2. In this geometry, named geometry 3, there are two phonon thermometers, with $\mathrm{Al}+\mathrm{Al}_x\mathrm{O}$ leads, at different distances from the heater, but placed on opposite sides of the heater. The conclusion from the experiments (data is not shown here) is that the temperature profile is not affected even if the thermometers are placed as far from each other as possible on the opposite sides of the heater. The same geometry 3 is also used for samples on top a 750 nm membrane. Hence the phonon thermometer pair M200a and M200b as well as M750a and M750b are each on top same membrane, but thermometers M40a-M40k are placed alone on top of separate membranes according to geometry 2.

In figures 7.4 (a) and (c) the input heating power versus local phonon temperature is shown in loglog-scale for samples M750a-b, M200a-b, M40f and M40h. The distance between the thermometer and the center of the heater is the same for all samples in each graph: (a) $R \sim 40$ μm and (c) $R \sim 100$ μm. At both distances the thickest membranes are clearly the coldest, which in other words means the highest thermal conductance. Samples on top 200 and 40 nm membranes behaves almost identically, but surprisingly, in Fig. 7.4 (a) the thermometer (M200a) on top 200 nm thick membrane is hotter than the thermometer (M40f) on top the thinnest membrane below 0.5 K. When the thermometer is further from the heater (see Fig. 7.4 (c)), the sample (M40h) on top the thinnest membrane is hottest over the whole studied temperature range, as expected intuitively.

When two arbitrary points, named 1 and 0, are at different temperatures T_1 and T_0 and $T_1 > T_0$, the heat flow between them has the form $P = K\left(T_1^n - T_0^n\right)$. The prefactor K and the exponent n depend on the nature of phonon transport, sample geometry and phonon dimensionality as discussed above. If $T_1 \gg T_0$, $P = KT_1^n$ and it is possible to study the exponent n again in more detail with the help of the

Table 7.1 Parameters for the measured samples. The parameters were measured by SEM and ellipsometer. M=suspended SiN_x membrane. d is the thickness of the membrane, R is the distance between the thermometer and the center of the heater, A is the area of the membrane, x the distance from the edge of the membrane and T_{bcs} temperature, where the saturation area starts in a calibration curve. The membrane of the sample M750 broke before the exact determination of the dimensions and the estimated error for R is ± 5 μm.

Sample	SiN_x d (nm)	R (μm)	A [(μm)^2]	x (μm)	T_{bcs} (K)
M750a	736	~40	646×601	-	0.218
M750b	736	~100	646×601	-	0.292
M200a	214	42	470×432	195	0.216
M200b	214	97	470×432	135	0.330
M40heater	46	-	440×391	-	-
M40a	43.0	12.2	403×450	212	0.300
M40b	41.5	14.5	392×429	199	0.265
M40c	40.3	15.9	451×477	223	0.250
M40d	44.5	24.2	380×433	187	0.230
M40e	39.0	36.5	536×503	207	0.400
M40f	44.1	37.6	485×444	177	0.140
M40g	41.5	71.7	456×493	163	0.230
M40h	40.0	97.1	521×486	144	0.300
M40i	45.0	134	446×395	3	0.400
M40j	44.0	148	559×510	112	0.300
M40k	41.0	182	390×438	66	0.405

logarithmic numerical derivative. In figure 7.4 (b) and (d) the exponent n versus the local phonon temperature from the graphs (a) and (c) is presented. We see that the temperature dependences measured on top 200 and 750 nm membranes behave almost identically, although the value of n depends slightly on the distance from the heater. This type of distance dependence was not studied in previous experiments. In Fig. 7.4 (b) ($R \approx 40$ μm) the exponent $n \approx 3.3$ for the samples M200a and M750a until 0.8 K, but for the sample M40f on top of the thin membrane $n \approx 3.3$ below and $n \approx 2.8$ above 0.38 K. When the thermometers are further from the heater, the exponent n has systematically higher values in each sample (see Fig. 7.4 (d)). Below 0.35 K the sample M40h on top 40 nm thick membrane has the highest value $n \approx 3.9$ while for the samples M750b and M200b $n \approx$ 3.4-3.5.

The temperature dependence of the thickest membrane (750 nm) agrees well with the data measured by Holmes *et. al* [55] in ~ 800 nm thick membranes in the

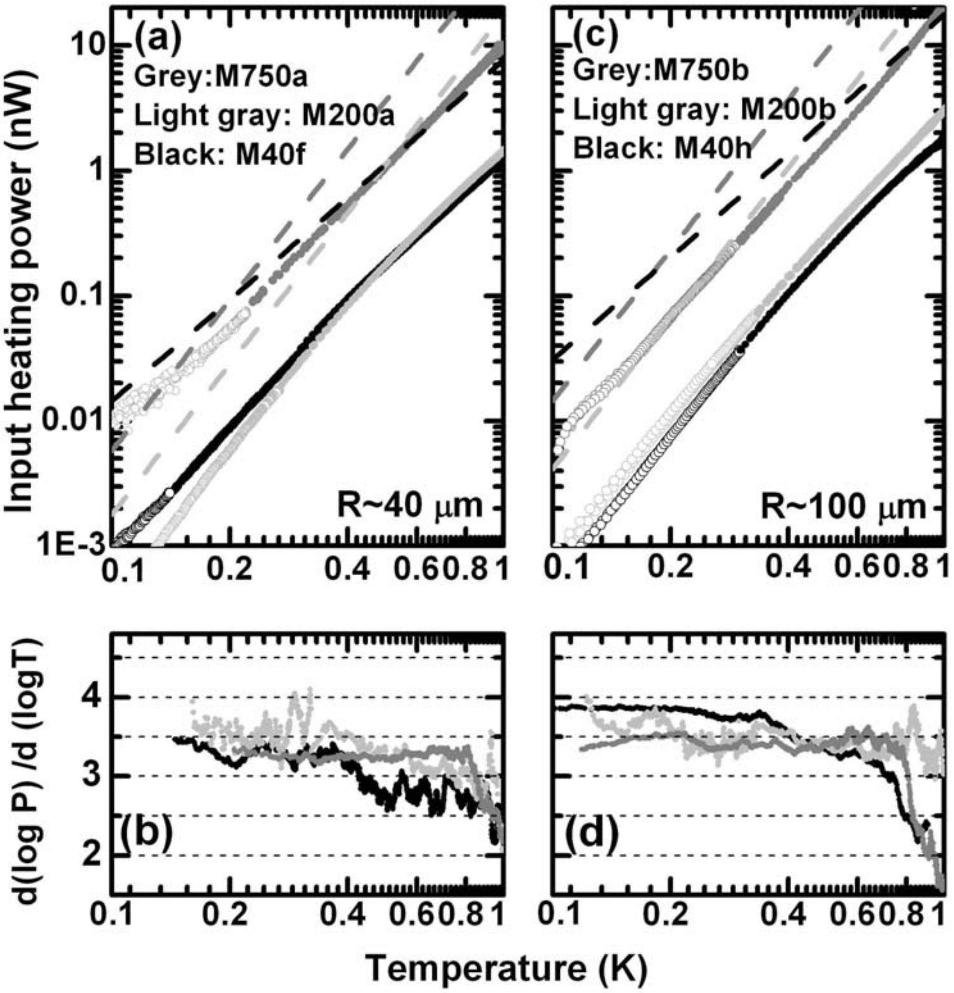

Figure 7.4 (a) and (c) Input heating power P versus local phonon temperature T_p. Open circles represent the saturation area in temperature analysis, and the exact value of the temperature, where the analysis method is changed, is shown in table 7.1. The distance from the origin is in Fig. (a) $R \approx 40$ μm and in Fig. (c) $R \approx 100$ μm for all samples in each graph. The grey, light grey and black dashed lines represent the specular limit for samples M750, M200 and M40 respectively. (b) and (d) The corresponding logarithmic numerical derivative from each curve. In Fig. (b) the data is limited to 0.156 K because of excessive noise in numerical derivative.

same temperature range. They reported that the exponent n =3.33 and we observe 3.3-3.4 depending on the distance R. In previous experiment by Leivo *et. al* [12] for a 200 nm thick membrane, quite similar set up was used, and their distance between the heater and the thermometer (both SINIS tunnel junctions) was $\sim$ 100 μm. However, their observed exponent n ~3 differing from our observation n ~3.4, for an unknown reason. In conclusion and consistently with previous measurements, we have not observed the exponent $n = 4$, which is predicted from the radiative phonon transport model in 3D.

To compare our experimental results to the specular limit of the phonon radiative transfer model, the sample geometry needs to be taking into account. If $T_{base} = 0$ K, the net radiative power emitted by the heater P_h and the thermometer P_t in steady state is

$$\begin{aligned} P_h &= P_{heat} + \alpha P_t \\ P_t &= \beta P_h, \end{aligned} \tag{7.4}$$

where $P_{heat} = IV$ is the input heating power and $\alpha = R_h/2R$ and $\beta = l/2\pi R$, where R is the radius of the heater and l the length of the thermometer. From the previous equations, we can solve P_t

$$P_t = \frac{l}{2\pi R}\left(1 - \frac{lR_h}{4\pi R^2}\right)^{-1} P_{heat} \equiv P_{rad}, \tag{7.5}$$

which on the other hand is the emitted power P_{rad} from the phonon radiative transfer model. By rewriting Eq. (7.5), we thus get

$$P_{heat} = \frac{2\pi R}{l}\left(1 - \frac{lR_h}{4\pi R^2}\right) P_{rad}. \tag{7.6}$$

According to our previous measurements discussed in chapter 6 [III] the 750 and 200 nm thick membranes are in 3D limit, so that the power flow in Eq. (7.6) is calculated by using P_{rad} in Eq. (7.2). However, the thinnest membranes are expected to be in the 2D limit, and in this case P_{rad} needs to be calculated from Eq. (7.3).

In Figs. 7.4 (a) and (c), the specular limit, as calculated from Eq. (7.6) is plotted as a dashed line for each sample. When the thermometers are closer to the heater in Fig. 7.4 (a), the specular limit is reached in the thickest membrane sample, M750a, at the lowest temperatures. This is in agreement with Holmes' [55] and Hoevers' [56] observations. However, if the thermometer is further, the ballistic limit is not reached. In the thinner membranes, M200 and M40, diffusive phonon transport seems to dominate regardless of the distance from the heater. Even at $T \sim 0.1$ K, ξ for the samples M200a and M40f are 0.2 and 0.1, respectively. By studying the deviation from the specular limit as a function of temperature, membrane thickness and distance, we can see that the deviation becomes larger as temperature increases, the membrane thickness decreases and on the other hand if the thermometer is further.

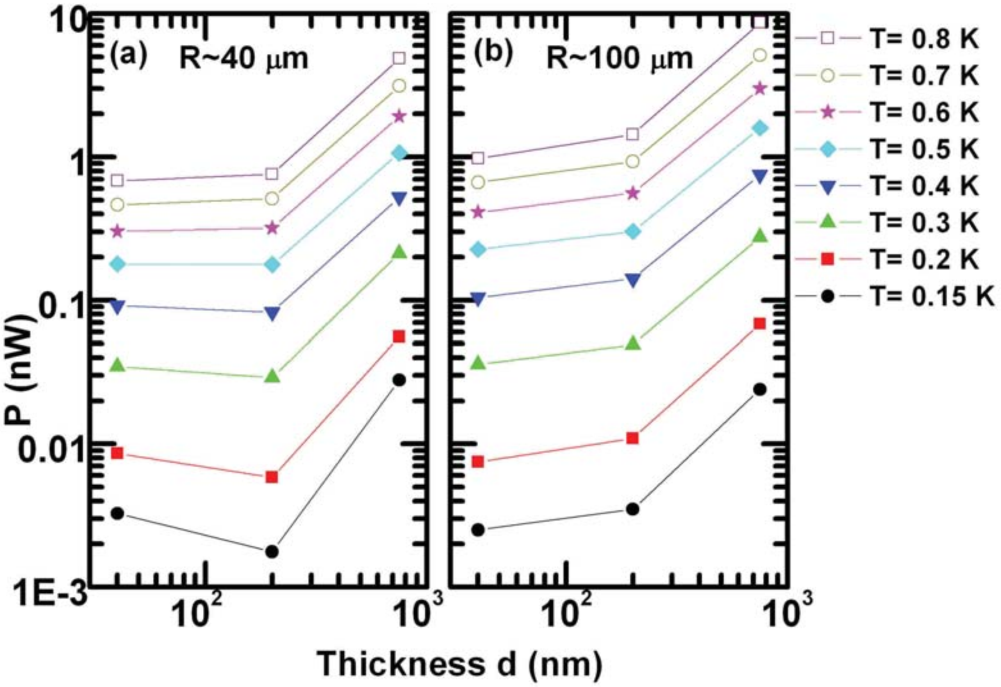

Figure 7.5 Measured input heating power P versus membranes thickness d at constant phonon temperature T_p. (a) Data from samples M40f, M200a and M750a. (b) Data from samples M40h, M200b and M750b.

In all cases, phonons undergo more scattering events and, hence, transport becomes more diffusive, which explains the increasing divergence.

As discussed in section 7.1 above, the radiatively emitted power for 3D phonons decreases linearly as a function of membrane thickness, but for 2D phonons $P \propto 1/\sqrt{d}$. In figures 7.5 (a) and (b) we show the input heating power versus the thickness of the membrane at constant temperatures from 0.15 K to 0.8 K for samples with $R \approx 40$ μm and $R \approx 100$ μm. Clearly, the data is not linear in either of the graphs and in Fig. 7.5 (a) a minimum below 0.5 K can be seen. This is in agreement with the theoretical result for Lamb modes in the 2D limit discussed in sections 7.1, which predicts a minimum for the thermal conductivity approximately at the dimensionality crossover thickness. The temperature, at which the minimum appears to measured data $T \sim 0.6$ K, is surprisingly close to the calculated value of the dimensionality crossover temperature, $T_c \approx 0.59$ K, for a 40 nm thick membrane, and also the observed T_c for the 30 nm thick membranes in previous experiments [III,IV]. Therefore we conclude that the dimensionality cross over is observed in this measurement. The obvious question that follows is, why is the minimum not observed in samples with the same membrane thickness, but the thermometer further away from the heater (Fig. 7.5 (b))?

According to the theory discussed in section 7.1 the minimum appears, if the heat transport can be explained by the phonon radiative transfer model. For other scattering mechanisms, for example for TLSs, it is not necessarily the case. The measured exponent for the temperature dependence of the P deviates from n =4, which implies that also an unknown scattering mechanism contributes to the heat transport. We have also observed that diffusive transport increases as the temperature is measured further away from the heater. Therefore, if the portion of the unknown scattering mechanism increases as a function of distance and if it does not depend on the properties of the a–mode the same way as the radiative model, the minimum is not necessarily observed.

We have also studied phonon transport as a function of distance in more detail for the thinnest membrane, $d \approx 40$ nm. Altogether 11 thermometers, M40a-M40k, are studied, and the distance of the thermometers was varied from 12.2 μm to 182 μm. One thermometer, M40i, is only 3 μm away from the edge of the membrane to study the effect of the edge. In figure 7.6 (a) and (c) the results are shown, in which P versus T_p is plotted in loglog-scale, and in Fig. 7.6 (b) and (d) the corresponding numerical logarithmic derivatives.

In Fig. 7.6 (a) the electron temperature of the heater (M40heater) is plotted, in addition to the measured data from the samples M40a-f, which are 12.2-37.6 μm away from the center. The dashed lines represent the data from the rest of the samples from Fig. (c). Generally, temperature decreases as a function of distance, but samples M40c and M40e are exceptions. The thermometer M40c (R =15.9 μm) is colder that thermometer M40d (R =24.2 μm) below 0.43 K even though the distance difference is obvious. The same effect is also observed for samples M40e (R =36.5 μm) and M40f (R =37.6 μm) and the crossover is at the same temperature $T \approx 0.43$ K. If we compare the thicknesses of the membranes, d is slightly smaller in the samples M40i and M40e compared to others. This actually confirms the result above that the thermal conductivity increases as the membranes thickness decreases in the 2D limit. The crossover temperature is the same for the sample pairs, because the thickness difference is for both $\Delta d \approx 5$ nm. At higher temperature, $T > 0.4$ K, the thermometers M40a-d start approaching the temperature of the heater and the data starts to bend strongly for all samples. The reason for this could be that, due to the short length of the heater, the dominant cooling mechanism for electrons at the

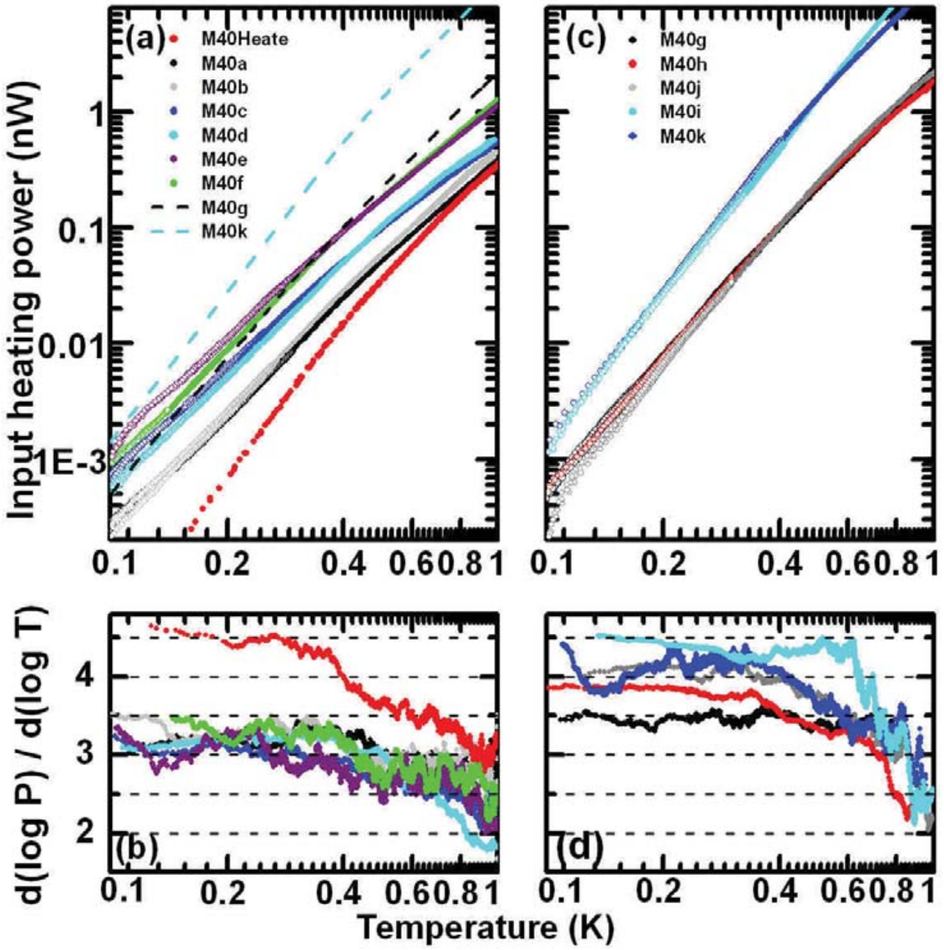

Figure 7.6 (a) P versus T_p. Data from the samples M40a-M40f and the electron temperature of the heater M40heater.(b) The corresponding logarithmic derivatives from the data in Fig. (a). (c) P versus T_p. Data from the samples M40g-M40k. (d) The corresponding logarithmic derivatives from the data in Fig.(c).

higher temperatures is quasiparticle heat transfer through the SN contacts instead of electron-phonon coupling. This drastically changes the temperature behavior of the heater [47] and naturally the power emitted to the membrane. This effect can be seen very clearly, when the exponent n is plotted as a function of temperature in Fig. 7.6 (b). Below $T \sim$ 0.4 K, n ~4.5 for the heater (M40heater), which is consistent with previous measurements discussed in chapter 6.2 [III, IV], and $n \sim$ 3.0-3.3 for the phonon thermometers. When $T >$ 0.4 K, the value of n decreases both in the heater and the phonon thermometers. This may indicate that the electron-phonon coupling starts to lose its dominance for the electron energy relaxation mechanism in the heater. The same effect can also be seen in Fig. 7.4 at higher temperatures.

In Fig. 7.6 (c) the data from the rest of the thermometers M40g-h is plotted, which are further form the heater $R \geq 71.7\ \mu$m. The data from the samples M40g, M40h and M40j collapse, which is unexpected, because the distance from the heater is doubled between the samples M40j ($R = 71.7\ \mu$m) and M40g ($R = 148\ \mu$m). Also compared with data nearer the heater in Fig. 7.6 (a), these samples behave strangely, as below 0.4 K the thermometers further are hotter than the thermometers nearer the heater. The difference in the membrane thicknesses does not explain this, because the thickness is not decreasing as the distance increases.

When the thermometer is closer to the edge of the membrane, it seems like the edge start to influence the heat transport. The distance from the heater is almost the same for the samples M40i and M40j (in Fig. 7.6 (c)), but M40i is very near the edge (3 μm). Clearly, the temperature is much lower in M40i than in M40j. The data from M40i also collapse with the data from the sample M40k although Rs differ by 26 %. The temperature dependence is also changing as a the distance from the edge decreases (see Fig. 7.6 (d)) and the exponent n seems to approach 4.5. It looks like the exponent n is also strongly affected by the distance from the edge. For example, the exponent for the samples M40i (n ~4.5) and M40j (n ~4.1) is clearly different even though the distance from the heater is almost the same.

In figure 7.7 (a) we plot the local phonon temperature versus the distance from the center for samples M40a-M40k (except the sample M40i). Now we can compare the measured temperature profiles with modeling in more detail way both for ballistic and diffusive transport. In the ballistic case, from Eq. (7.6) we get

$$T = \left[\frac{Bl}{2\pi R} \frac{1}{\left(1 - \frac{lR_h}{4\pi R^2}\right)} \right]^{(1/n)}, \tag{7.7}$$

where a effective model $P_{rad} = aT^n$ with a fitting constant a is assumed and $B = P_{heat}/a$. In a diffusive case, the radial heat flow is

$$P = -S(r)\kappa(T)\frac{dT}{dr}, \tag{7.8}$$

where $S(r) = 2\pi Rd$ is the cross sectional area for the heat transport for our geometry. If we assume $\kappa(T) = \alpha T^m$, in which α is constant, and integrate equation (7.8), we get

$$\begin{aligned} -\int_{r_0}^{r} \frac{P}{2\pi r d} dr &= \int_{T_0}^{T} \alpha T^m dT \\ \frac{P}{2\pi d}\ln\left(\frac{\mathrm{r_0}}{\mathrm{r}}\right) &= \frac{\alpha}{\mathrm{m+1}}\left(\mathrm{T^{m+1} - T_0^{m+1}}\right), \end{aligned} \tag{7.9}$$

where point(r_0, T_0) is known. From Eq. (7.9) above we can solve $T(R)$ in the diffusive case:

$$T = \left[T_0^{m+1} + \frac{(m+1)P}{2\pi\alpha d}\right]^{1/(m+1)}, \tag{7.10}$$

where α is a fitting constant.

The temperature profile is studied for the low and high values of the input heating power in Fig.7.7 (b) by using the ballistic and diffusive model explained above. At the lower temperatures the membrane is in the 2D limit and the measured data points have some deviations due to the membrane thickness variations. In the 3D limit, where $P \propto d$, the dependence is weaker and hence the deviations are smaller. If we compare the shape of the theoretical curves, clearly the ballistic model has more qualitatively the shape, which correspond the measured data. Also the plateau at $R > 40$ μm in temperature can be understood with the ballistic model, whereas in the diffusive model the temperature decreases almost linearly. However, at $R > 40$ μm the ballistic model predicts lower absolute temperatures than the measurement. If we add one more fitting constant C to Eq. (7.7) ($T = (Bl/2\pi R(1 - lR/(4\pi R^2)))^{1/n} + C$), the ballistic model agrees with the data better. Note that we do not understand the physical meaning of C at the moment. This implies that the ballistic portion of the transport dominates in the $T(R)$ behaviour.

In conclusion, it seems that different transport mechanisms affect in the observables in heat transport, such as the temperature dependence, spatial profile and the absolute values of T, different ways. We have observed that the portion of diffusive transport increases as a function of temperature, membrane thickness and distance from the heat source, although the ballistic limit is reached in the thickest membrane at the lowest temperatures, when the thermometer is not too far from the heater. This diffusive transport must also consist of a contribution from an unknown scattering mechanism, because the observed exponent for temperature dependence deviates from $n = 4$ in 3D limit and from $n = 3 - 2.5$ in 2D limit, as expected for the boundary scattering. However, we have also observed the minimum in thermal conductance as a function of membrane thickness, which strongly implies that boundary scattering influences the heat transport. The specular limit is not observed in

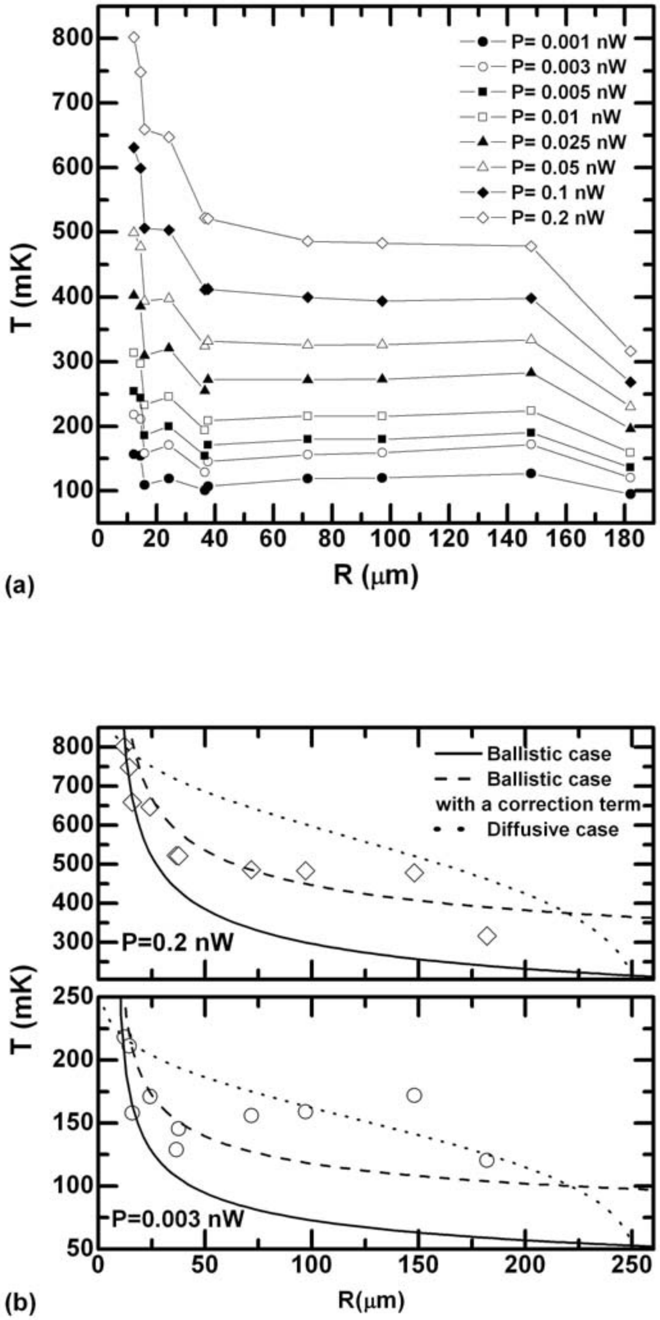

Figure 7.7 The local phonon temperature T_p versus the distance from the center R at the constant input heating power P for samples M40a-M40k except M40i. (b) In figure above the input heating power is $P = 0.2$ nW and below P =0.003 nW. Black solid line: the ballistic model from Eq. (7.7), in which the exponent $n = 3$, $B(0.003nW) = 1.6 \times 10^7$ and $B(0.2nW) = 1.08 \times 10^9$. Black dashed line: the ballistic model from Eq. (7.7) added with a fitting constant C: $C(0.003nW) = 45$ and $C(0.2nW) = 150$. Black dotted line: the diffusive model from Eq. (7.10) with $m = 3$, $(r_0, T_0) =$ (12,2 μm, 802 mK) and $(r_1, T_1) =$ (250 μm, 50 mK), which is the edge of the membrane. If we use $n, m = 4$, the curves changes only slightly.

the 2D limit, but it seems like the temperature profile can be qualitatively explained by a ballistic model. It is clear that according to our experiments, heat transport in suspended silicon nitride membranes is affected by several scattering mechanisms.

Chapter 8

Conclusions

In this thesis thermal properties of low dimensional structures were experimentally studied at low temperatures with the help of tunnel junction thermometry and the Joule heating technique. The main objects of study were electron-phonon coupling in disordered thin metal films and phonon transport in suspended silicon nitride membranes. Our aim has been to clarify the effect of the phonon dimensionality, *i.e.* the effect of boundaries to the phonon modes and the transition from 3D to 2D phonons. The dimensionality cross over had not been observed before this work even though it is fabricationally a standard procedure to create the low dimensional environments for nanoscale applications and devices. The main conclusion here is that the nature of thermal phenomena can differ drastically in lower dimensional structures compared to bulk behaviour, and sometimes surprisingly advantageous ways.

First, we have studied both numerically and experimentally the thermal gradients in well-conducting mesoscopic metal wires on top 3D bulk substrates below 1 K, with a non-uniform Joule heating technique. We have observed that there are significant thermal gradients in copper and aluminum manganese wires even though the non-heated portion of the wire (10 μm) is less than the electron-phonon scattering length. The measured data agrees well with a model, in which the electronic thermal conductivity obeys the Wiedemann-Franz law and the electrons are cooled due to the electron-phonon coupling. The phenomena is surprisingly strong, and has a crucial effect on studies of thermal properties and thermometry at low temperatures, where the electron-phonon coupling is the dominant electron energy relaxation mechanism.

Next we have studied the electron-phonon coupling in thin metal films at sub-Kelvin temperatures in 3D and 2D phonon environments. We fabricated identical samples on top of 30, 200 and 750 nm thick free-standing SiN_x membranes and Si bulk substrates to see clearly the effect of phonon dimensionality. With these samples, we demonstrated for the first time that the temperature dependence of the electron-phonon coupling indeed changes as expected from the theory, and, surprisingly, the strength of the interaction becomes stronger compared to the 3D phonon spectrum in thicker membranes and bulk samples below $\sim$ 0.5 K. Also a systematic measurement series was performed for Cu wires on top bulk Si substrate as a function of disorder, *i.e.* electron mean free path, by varying the film thickness from 14 nm to 90 nm. We observed that the electron-phonon coupling behaves qualitatively as predicted by the advanced theories, which has not been widely established experimentally.

In the latter part of this thesis, we have studied phonon transport in suspended silicon nitride membranes, which are widely used structures, for example in detector applications below 1 K. We have measured heat transport in 750, 200 and 40 nm thick membranes by detecting the local phonon temperature with tunnel junction thermometers at different distances, R, from a radially symmetric Cu thin film heater in the middle of the membrane. For the thickest membrane and $R \sim$40 μm, our data is in agreement with previous measurements and the ballistic limit is reached at $T \sim$ 0.15 K. However, we have observed that the portion of the diffusive transport increases as temperature rises, the membrane thickness decreases and when the thermometer is further from the heater. However, the observed exponent for the temperature dependence is not $n = 4$ in the 3D limit and $n = 3 - 2.5$ for the 2D limit as expected for the case of surface scattering, which means that also an unknown scattering mechanism plays a role. According to the previous measurements, the 40 nm thick membrane is expected to be in the 2D limit and the dimensionality crossover from 3D to 2D phonons is confirmed by observing a minimum in the thermal conductance as a function of temperature for the first time. Below 0.5 K, the thermal conductance is indeed better in the 40 nm than the 200 nm thick membrane. However this intuitively surprising result is expected theoretically, and it implies that boundary scattering has the effect on heat transport. We have also studied the phonon temperature profile as a function of distance in more detailed for the thinnest membranes. The dependence is qualitatively ballistic, but the data and the model are not in clear agreement. We have also measured that in the thinnest membranes the edge of the membrane has a strong effect on the temperature profile near by it, changing the absolute value of the temperature and the exponent n drastically.

Bibliography

[I] This thesis article **A.I.**

[II] This thesis article **A.II.**

[III] This thesis article **A.III.**

[IV] This thesis article **A.IV.**

[V] This thesis article **A.V.**

[1] MANDL, F., *Statistical Physics* (John Wiley & Sons, Great Britain, 1999), 2nd ed.

[2] GIAZOTTO, F., HEIKKILÄ, T., LUUKANEN, A., SAVIN, A., AND PEKOLA, J., *Opportunities for mesoscopics in thermometry and refrigeration: Physics and applications*. Rev. Mod. Phys. **78** (2006) 217.

[3] MOSELEY, S., MATHER, J., AND MCCAMMON, D., *Thermal detectors as x-ray spectrometers*. J. Appl. Phys. **56** (1984) 1257.

[4] ENSS, C., *Cryogenic Particle Detection* (Springer, Germany, 2005).

[5] DOLAN, G., *Offset masks for lift-off photoprocessing*. Appl. Phys. Lett. **31** (1977) 337.

[6] FRANSSILA, S., *Introduction to Microfabrication* (McGraw-Hill, Singapore, 1996), 2nd ed.

[7] PEKOLA, J. AND KAUPPINEN, J., *Insertable dilution refrigerator for characterization of mesoscopic samples*. Cryogenics **34** (1994) 843.

[8] ZORIN, A., *The thermocoax cable as the microwave frequency filter for single electron circuits*. Rev. Sci. Instrum. **66** (1995) 4296.

[9] GIAEVER, I., *Electron tunneling between two superconductors*. Phys. Rev. Lett. **5** (1960) 464.

[10] TINKHAM, M., *Introduction to Superconductivity* (McGraw-Hill, Singapore, 1996), 2nd ed.

[11] NAHUM, M., EILES, T., AND MARTINIS, J., *Electronic microrefrigerator based on a normal-insulator-superonductor tunnel junction*. Appl. Phys. Lett. **65** (1994) 3123.

[12] LEIVO, M. AND PEKOLA, J., *Thermal characteristics of silicon nitride membranes at sub-kelvin temperatures*. Appl. Phys. Lett. **70** (1998) 1305.

[13] CLARK, A., MILLER, N., WILLIAMS, A., RUGGIERO, S., HILTON, G., VALE, L., BEALL, J., IRWIN, K., AND ULLOM, J., *Cooling of bulk material by electron-tunneling refrigerators*. Appl. Phys. Lett. **86** (2005) 173508.

[14] SCHMIDT, D., YUNG, C., AND CLELAND, A., *Nanoscale radio-frequency thermometry*. Appl. Phys. Lett. **83** (2003) 1002.

[15] DYNES, R., J.P.GARNO, HERTEL, G., AND ORLANDO, T., *Tunneling study of superconductivity near the metal insulator transition*. Phys. Rev. Lett. **53** (1984) 2437.

[16] PEKOLA, J., HEIKKILÄ, T., SAVIN, A., FLYKTMAN, J., GIAZOTTO, F., AND HEKKING, F., *Limitations in cooling electrons by normal metal-superconductor tunnel junction*. Phys. Rev. Lett. **92** (2004) 056804.

[17] TOPPARI, J., KÜHN, T., HALVARI, A., AND PARAOANU, G., *Method for finding the critical temperature of the island in a set structure*. J. Phys.:Conf. Ser. **150** (2009) 022088.

[18] RAJAURIA, S., GANDIT, P., FOURNIER, T., HEKKING, F., PANNETIER, B., AND COURTOIS, H., *Andreev current-induced dissipation in a hybrid superconducting tunnel junction*. Phys. Rev. Lett. **100** (2008) 207002.

[19] KOPPINEN, P., KÜHN, T., AND MAASILTA, I., *Effects of charging energy on sinis tunnel junction thermometry*. J. Low. Temp. Phys **154** (2009) 179.

[20] COURT, N., FERGUSON, A., AND CLARK, R., *Energy gap measurement of nanostructured aluminium thin films for single cooper-pair devices*. Supercond. Sci. Technol. **21** (2008) 015013.

[21] MESERVEY, R. AND TEDROW, P., *Properties of very thin aluminum films*. J. Appl. Phys. **42** (1971) 51.

[22] REIZER, M. Y., *Electron-phonon relaxation in pure metals and superconductors at very low temperatures*. Phys. Rev. B **40** (1989) 5411.

[23] Wellstood, F., Urbina, C., and Clarke, J., *Hot-electron effect in metals*. Phys. Rev. B **49** (1994) 5942.

[24] Gantmakher, V., *The experimental study of electron-phonon scattering in metals*. Rep. Prog. Phys **37** (1974) 317.

[25] Sergeev, A. and Mitin, V., *Electron-phonon interaction in disordered conductors: Static and vibrating scattering potentials*. Phys. Rev. B **61** (2000) 6041.

[26] Roukes, M., Freeman, M., Germain, R., Richardson, R., and Ketchen, M., *Hot electron and energy transport in metals at millikelvin temperatures*. Phys. Rev. Lett. **55** (1985) 422.

[27] Kanskar, M. and Wybourne, M., *Measurement of the acoustic-phonon mean free path in a free-standing metal film*. Phys. Rev. Lett. **50** (1994) 2123.

[28] Echternach, P., Thoman, M., Gould, C., and Bozler, H., *Electron-phonon scattering rates in disordered metallic films below 1 k*. Phys. Rev. B **46** (1992) 10339.

[29] Yung, C., Schmidt, D., and Cleland, A., *Thermal conductance and electron-phonon coupling in mechanically suspended nanostructures*. Appl. Phys. Lett. **81** (2002) 31.

[30] Vinante, A., Falferi, P., Mezzena, R., and Mück, M., *Hot-electron effect in palladium thin films*. Phys. Rev. B **75** (2007) 104303.

[31] Wu, C., Jian, W., and Lin, J., *Electron-phonon scattering times in crystalline disordered titanium alloys between 3 and 15 k*. Phys. Rev. B **57** (1998) 11 232.

[32] Zhong, Y. and Lin, J., *Observation of a linear mean-free-path dependence of the electron-phonon scattering in thick aupd films*. Phys. Rev. Lett. **80** (1998) 588.

[33] Gerhenson, M., Dong, D., Sato, T., Karasik, B., and Sergeev, A., *Millisecond electron-phonon relaxation in ultrathin disordered metal films at millikelvin temperatures*. Appl. Phys. Lett. **79** (2001) 2049.

[34] Komnik, Y. F., Kashirin, V. Y., Belevtsev, B., and Beliaev, E. Y., *Temperature variation of the time of inelastic electron relaxation in disordered bismuth films*. Phys. Rev. B **50** (1994) 15298.

[35] Taskinen, L. and Maasilta, I., *Improving the performance of hot-electron bolometers and solid state coolers with disordered alloys*. Appl. Phys. Lett. **89** (2006) 143511.

[36] CEDER, R., AGAM, O., AND OVADYAHU, Z., *Nonohmicity and energy relaxation in diffusive two-dimensional metals*. Phys. Rev. B **72** (2005) 245104.

[37] BERGMANN, G., *Nonequilibrium in metallic microstructures in the presence of high current density*. Phys. Rev. B **41** (1990) 7386.

[38] GELLER, M., *Local phonon density of states in an elastic substrate*. Phys. Rev. B **70** (2004) 205421.

[39] QU, S.-X., CLELAND, A., AND GELLER, M., *Hot electrons in low-dimensional phonon systems*. Phys. Rev. B **70** (2004) 205421.

[40] AULD, B., *Acoustic Fields and Waves in Solids* (Robert E. Krieger Pub., Malabar, 1990), 2nd ed.

[41] GRIMSDITCH, M., BHADRA, R., AND SCHULLER, I., *Lamb waves in unsupported thin films: A brilluin scattering study*. Phys. Rev. Lett. **58** (1987) 1216.

[42] BELITZ, D. AND SARMA, S. D., *Inelastic phase-coherence time in thin metal films*. Phys. Rev. B **36** (1987) 7701.

[43] JOHNSON, K., WYBOURNE, M., AND PERRIN, N., *Acoustic-mode coupling and electron heating in thin metal films*. Phys. Rev. B **50** (1994) 2035.

[44] BERMAN, R., *Thermal Conduction in Solids* (Clarendon Press, Oxford, 1979).

[45] ANDREEV, A., *The thermal conductivity of the intermediate state in superconductor*. Soviet Physics JETP **19** (1964) 1228.

[46] BLONDER, G., TINKHAM, M., AND KLAPWIJK, T., *Transition from metallic to tunneling regimes in superconducting microconstrictions: Excess current, charge imbalance and supercurrent conversion*. Phys. Rev. B **25** (1982) 4515.

[47] HOFFMANN, C., LEFLOCH, F., AND SANQUER, M., *Inelastic relaxation and noise in s/n/s junctions*. Eur. Phys. J. B **25** (2002) 629.

[48] PIERRE, F., ANTHORE, A., POTHIER, H., URBINA, C., AND ESTEVE, D., *Multiple andreev reflections revealed by the energy distribution of quasiparticles*. Phys. Rev. Lett. **86** (2001) 1078.

[49] TIMOFEEV, A., HELLE, M., MESCHKE, M., MÖTTÖNEN, M., AND PEKOLA, J., *Electronic refrigeration at the quantum limit*. Phys. Rev. Lett. **102** (2009) 200801.

[50] DiTusa, J., Lin, K., M.S.Isaacson, and Parpia, J., *Role of phonon dimensionality on electron-phonon scattering rates*. Phys. Rev. Lett. **68** (1992) 1156.

[51] Kwong, Y., Lin, K., Isaacson, M., and Parpia, J., *An attempt to observe phonon dimensionality crossover effect in the inelastic scattering rate of thin free-standing aluminum films*. J. Low. Temp. Phys. **88** (1992) 261.

[52] Kühn, T., Anghel, D., Pekola, J., Manninen, M., and Galperin, Y., *Heat transport in ultra-thin dielectric membranes and bridges*. Phys. Rev. B **70** (2004) 125425.

[53] Taskinen, L., *Thermal Properties of Mesoscopic Wires and Tunnel Junctions*, Ph.D. thesis, University of Jyväskylä (2006).

[54] Ashcroft, N. and Mermin, N., *Solid State Physics* (Saunders College Publishing, USA, 1976).

[55] Holmes, W., Gildemeister, J., Richards, P., and Kotsubo, V., *Measurements of thermal transport in low stress silicon nitride films*. Appl. Phys. Lett. **38** (1998) 2250.

[56] Hoevers, H., Ridder, M., Germeau, A., Bruijn, M., and Korte, P., *Radiative ballistic phonon transport in silicon-nitride membranes at low temperatures*. Appl. Phys. Lett. **86** (2005) 251903.

[57] Woodcraft, A., Sudiwala, R., Wakui, E., Bhatia, R., Bock, J., and Turner, A., *Thermal conductance measurements of a silicon nitride membranes at low temperatures*. Physica B **284-288** (2000) 1968.

[58] Zink, B. L. and Hellman, F., *Specific heat and thermal conductivity of low-stress amorphous si-n membranes*. Solid State Communications **129** (2004) 1999.

[59] Casimir, H., *Note on the conduction of heat in crystals*. Physica (Amsterdam) **5** (1938) 495.

[60] Ziman, J., *Electrons and Phonons: The Theory of Transport Phenomena in Solids* (Clarendon, Oxford, 1960).

[61] Klitsner, T., VanCleve, J., Fisher, H., and Pohl, O., *Phonon radiative heat transfer and surface scattering*. Phys. Rev. B **38** (1988) 7576.

[62] Kühn, T. and Maasilta, I., *Ballistic phonon transport in dielectric membranes*. Nucl. Instr. and Meth. **559** (2006) 724.

[63] KÜHN, T., *Phononic Transport in Dielectric Membranes*, Ph.D. thesis, University of Jyväskylä (2007).

[64] PHILIPS, W., *Tunneling states in amorphous solids*. J. Low Temp. Phys. **7** (1972) 351.

[65] KÜHN, T., ANGHEL, D. V., GALPERIN, Y. M., AND MANNINEN, M., *Interaction of lamb modes with two-level systems in amorphous nanoscopic membranes*. Phys. Rev. B **76** (2007) 165425.

[66] WYBOURNE, M., EDDISON, C., AND KELLY, M., *Phonon boundary scattering at a silicon-sapphire interface*. J. Phys. C:Solid State Phys. **17** (1984) L607.